EYE-CLIMA
Verifying emissions of climate forcers

# Inversions of F-gases

## DELIVERABLE 3.6


| | |
|---|---|
| **Author(s):** | Seyed Omid Nabavi, Martin Vojta, Andreas Stohl |
| **Date of submission:** | 02-07-2026 |
| **Version:** | 01 |
| **Responsible partner:** | University of Vienna |
| **Deliverable due date:** | 30-06-2025 |
| **Dissemination level:** | Public |



| | |
|---|---|
| **Call:** | HORIZON-CL5-2022-D1-02 |
| **Topic:** | Climate Sciences and Responses |
| **Project Type:** | Research and Innovation Action |
| **Lead Beneficiary:** | NILU - Norsk Institutt for Luftforskning |



This project has received funding from the European Union's Horizon Europe research and innovation programme under grant agreement No 101081395

## Document History

| Version | Date | Comment | Modifications made by |
|---|---|---|---|
| 0.1 | 05-06-2026 | First Draft | Seyed Omid Nabavi, Martin Vojta, Andreas Stohl, Antoine Berchet, and Rona Thompson |
| 0.2 | 30-06-2026 | Draft sent to review | Seyed Omid Nabavi, Martin Vojta, Andreas Stohl, Antoine Berchet, and Rona Thompson |
| 0.3 | 15-06-2026 | Internal review | Antoine Berchet, Rona Thompson |
| 1.0 | 01-07-2026 | Final version | Seyed Omid Nabavi |

This project has received funding from the European Union's Horizon Europe research and innovation programme under grant agreement No 101081395

## Summary

The overall purpose of this deliverable is to determine the emissions in Europe and elsewhere of key F-gases. The hydrofluorocarbons (HFCs) HFC-23, HFC-32, HFC-125 and HFC-134a as well as $SF_6$ were selected for this study on the basis of their magnitude of emissions and global warming potential. While bottom-up inventories of all these gases exist and national emissions in Europe need to be reported to UNFCCC, it is known that these estimates have major shortcomings. Therefore, it is important to verify these emissions and improve them on the basis of available atmospheric mole fraction measurements.

For this purpose, we used a top-down approach based on inverse modelling. Inverse modelling combines a priori emission information, an atmospheric transport model and atmospheric mole fraction measurements in an optimal way, considering uncertainties in all these components. We used the Bayesian inversion framework FLEXINVERT+, the atmospheric transport model FLEXPART, and measurement data from various sources.

Although not part of the work plan and thus not reported here, we also studied the perfluorocarbons $CF_4$ and $C_2F_6$ as the topic of a master thesis. Results of this analysis can be found in the paper by Püschel et al. (2025), which currently is under review in Atmospheric Chemistry and Physics.

This project has received funding from the European Union's Horizon Europe research and innovation programme under grant agreement No 101081395

# TABLE OF CONTENTS



This project has received funding from the European Union's Horizon Europe research and innovation programme under grant agreement No 101081395

# 1. Introduction

Hydrofluorocarbons (HFCs) are synthetic, fluorinated gases (F-gases) first produced in the 1990s to replace ozone-depleting substances such as chlorofluorocarbons (CFCs) and hydrochlorofluorocarbons (HCFCs), which were phased out under the Montreal Protocol and its subsequent amendments. They are widely used as refrigerants in cooling and air conditioning systems and also appear in foam insulation, aerosol products, fire suppression systems, and certain industrial solvents. HFCs do not deplete ozone but are potent greenhouse gases because of high GWPs from strong radiative efficiency and long lifetimes (Kikstra et al., 2022). HFC-23, a byproduct of HCFC 22 production, originates mostly from industrial point sources and has a 100-year GWP ($GWP_{100}$) of 14600. Its atmospheric lifetime is about 228 years, the longest among common HFCs. HFC-125, HFC-32, HFC-134a, and HFC-143a have $GWP_{100}$ values of about 3740, 771, 1530, and 5810 and atmospheric lifetimes of approximately 30, 5.4, 14, and 51 years, respectively and are emitted mainly from diffuse (areal) sources. These emissions arise from leaks and losses during the use, maintenance, or disposal of millions of distributed products containing these gases. Sulfur hexafluoride ($SF_6$) has the highest GWP of all known greenhouse gases ($GWP_{100}$ = 24700), and current estimates of its atmospheric lifetime range between 850 and 1280 years (WMO, 2022). Due to its high stability, it is used mainly as an insulator for electric equipment in the power industry (e.g. Cui et al. (2024)), with emissions occurring during equipment leakage, failures, maintenance, and decommissioning.

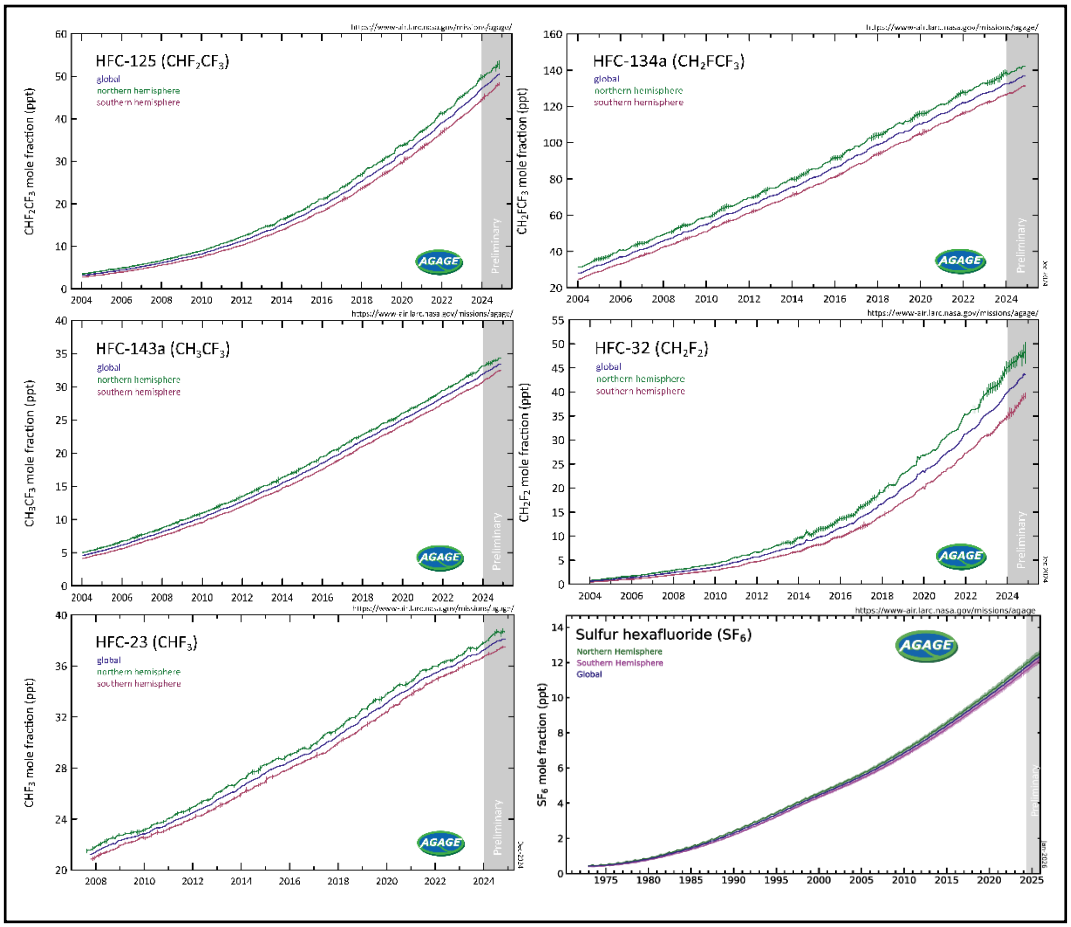


*Figure 1. AGAGE hemisphere-averaged time series of HFC-125, HFC-134a, HFC-143a, HFC-32, HFC-23, and $SF_6$. Points represent monthly mean mole fractions derived from observations at Zeppelin, Mace Head, Tacolneston, Jungfraujoch, Trinidad Head, Ragged Point, Cape Matatula, and Kennaook/Cape Grim. Error bars denote the ±1$\sigma$ of the monthly mean as reported by AGAGE. We acknowledge AGAGE for providing the original figure, derived from post-processing of HFC and $SF_6$ measurements.*

This project has received funding from the European Union's Horizon Europe research and innovation programme under grant agreement No 101081395

AGAGE observations (Prinn et al., 2018) show sustained growth in atmospheric HFC mole fractions, with multi-year variability, distinct recent growth rates, and clear hemispheric contrasts (Fig. 1). Since the beginning of study period 2014, AGAGE globally averaged HFC mole fractions have increased at distinct rates: HFC-134a has risen steadily by roughly 5 ppt $yr^{-1}$; HFC-125 and HFC-32 by about 3 ppt $yr^{-1}$ with a noticeable acceleration in the early 2020s; HFC-143a by approximately 1.5 ppt $yr^{-1}$; and HFC-23 by about 1 ppt $yr^{-1}$. Consistent with Northern Hemisphere–weighted emissions and species lifetimes, the mean NH–SH difference is largest for the shorter-lived HFC-32, moderate for HFC-125, HFC-143a, and HFC-134a, and smallest for the very long-lived HFC-23.

Global $SF_6$ mole fractions have almost tripled since the late 1990s, while atmospheric growth rates increased to roughly 0.4 ppt $yr^{-1}$. $SF_6$ is regulated under the Kyoto protocol, while the Kigali Amendment to the Montreal Protocol (2016) focuses specifically on hydrofluorocarbons (HFCs). The objective of the Kigali Amendment is an 85% reduction in HFC production and consumption in most developed nations between 2019 and 2036, with developing countries to follow a phased reduction schedule by 2047. Achieving these targets could reduce total synthetic greenhouse gas radiative forcing by roughly 26% by 2050 relative to 2012 levels (Rigby et al., 2014). Complementing these international treaties, the European Union (EU) has implemented additional measures to curb emissions of HFCs and other F-gases, including perfluorocarbons (PFCs) and $SF_6$ (Manning et al., 2021). The EU regulation (No. 842/2006, EU 2006) set rules for the containment, recovery, use, and reporting of F-gases. It banned the use of $SF_6$ in vehicle tires (starting in 2007) and in large-scale magnesium die-casting (starting in 2008), as well as in soundproof windows and footwear. The 2006 Mobile Air Conditioning (MAC) Directive introduced a phased ban on HFCs with 100-year global warming potentials ($GWP_{100}$) exceeding 150 in passenger cars and light commercial vehicles, effectively prohibiting the use of HFC-134a in all new vehicle models sold in the EU from January 2017 onward (Directive 2006/40/EC (MAC Directive)). The 2014 F-gas Regulation (No.517/2014, EU, 2014)), in force since January 2015, established a progressive, quota-based system designed to cut EU F-gas emissions by two-thirds by 2030. It restricted $SF_6$ use, required leak detection systems for electrical switchgear by 2017 and banned it from recycling magnesium alloys by 2018. The new regulation form 2024 (No 2024/590, EU 2024) accelerates the phase-down of HFCs toward an almost complete phase-out by 2050 and further tightens restrictions on $SF_6$.

Understanding how policies influence the atmospheric abundance of F-gases is crucial for policymakers, as it enables an accurate assessment of both policy effectiveness and emissions of these potent greenhouse gases. Emission quantification can be approached using two complementary methods: bottom-up (BU) and top-down (TD). BU methods enable sector-resolved estimates and fine spatial attribution, making them well suited for source apportionment and compliance assessment. However, BU inventories often carry substantial and difficult-to-characterize uncertainties arising from assumptions in activity data, emission factors, and reporting practices. Among these, emission factors have been identified as a major source of uncertainty in BU estimates (Flerlage et al., 2021). By constraining emissions through atmospheric observations, TD estimates serve as an independent means to reduce the uncertainties inherent in bottom-up estimates. However, they also face non-trivial sources of uncertainty. A comparison of four top-down inversion systems applied to HFC-125, HFC-134a, and $SF_6$ emissions over Europe showed that country-level estimates often fall outside each system's formal analytical uncertainty range, suggesting that parametric and structural uncertainties dominate the total uncertainty in these systems (Brunner et al., 2017). In this deliverable report, we present the F-gas inversions and their associated uncertainties with respect to the choice of parameter inputs for priori emissions and observational datasets, assumed prior and observational uncertainties, error correlation structures, treatment of baseline (background) concentrations, and spatial inversion resolution. It should be noted that the inversions of HFCs and $SF_6$ were conducted within two separate research efforts and largely over non-overlapping time periods. While we aimed to maintain a consistent framework, some minor differences in the presentation and layout of results between the two cases are unavoidable. The

This project has received funding from the European Union's Horizon Europe research and innovation programme under grant agreement No 101081395

reason for quantifying $SF_6$ and HFC emissions separately are that the inversion system was first systematically tested for $SF_6$, which is the species with the largest available measurement data set. Only thereafter, inversions for the HFCs were performed.

# 2. Methodology

This section describes the top-down inversion framework, the key inputs, and the way we quantify and reduce uncertainty. We present the core Bayesian inversion used to estimate emissions, followed by post-hoc consistency constraints for non-negativity and global total emissions. As already noted, HFC and $SF_6$ inversions were run separately from each other, as we used $SF_6$, the species with the largest number of available observations, to refine our inversion setup (Vojta et al., 2024; Vojta et al., 2025). These inversions were, therefore, conducted first, followed by the HFC inversions. For the latter approach, only a limited number of additional improvements were introduced. These included the application of Latin hypercube sampling for uncertainty quantification and the use of the recently updated FLEXPART-LCM (FP-LCM) to simulate the baseline, replacing its predecessor FLEXPART-CTM. We focus this description on the methodology used for the HFC-inversions but note differences to the $SF_6$ inversion setup.

## 2.1 Bayesian inversion framework

The atmospheric inverse modelling framework used in this study, FLEXINVERT+, is designed for top-down estimation of greenhouse gas (GHG) emissions. The system is described in detail by Thompson and Stohl (2014) and its application to F-gases is demonstrated by Vojta et al. (2024). The methodology is based on a Bayesian inversion approach, which statistically refines the target variables $x$ (i.e., the emission vector) by constraining them through both the observational data $y^0$ (top-down constraint) and their prior estimates $x_b$ (bottom-up constraint) linked by a linear forward operator, as described in subsection 2.4.2. Gaussian-distributed errors are assumed between the a priori and a posteriori emissions (Eq. 1) and between the observations and the simulated mole fractions (Eq. 2),

$$(1)\ P^x(x) = \frac{1}{\sqrt{2\pi|B|}} exp\left(\frac{-1}{2}(x - x_b)^{TB^{-1}}(x - x_b)\right)$$

$$(2)\ P^y(x) = \frac{1}{\sqrt{2\pi|R|}} exp\left(\frac{-1}{2}(y^0 - Hx)^{TR^{-1}}(y^0 - Hx)\right)$$

Here, the a priori error covariance matrix $B$ quantifies uncertainties in the baseline and a priori emission estimates along its diagonal, while its off-diagonal terms describe spatial correlations between grid cells. The observation error covariance matrix $R$ represents uncertainties in the observation space arising from measurement errors, transport modelling errors projected into the observation space, and representation errors. Using Bayes' theorem, $P(x|y) \propto P(y|x)P(x)$, we derive the a posteriori Gaussian probability distribution for emission error uncertainty. The cost function, defined as the negative logarithm of $P(x|y)$, is minimized to determine the optimal state of emissions, $x$, balancing observational and prior uncertainties. The minimization problem is analytically solvable (Eq. 3) because the sensitivity matrix $H$ provides a linear mapping from the emission vector to the observations. Analytical inversion offers two key benefits: (1) a complete characterization of the a posteriori error covariance matrix (Katharopoulos et al., 2023), and (2) guaranteed convergence to the global minimum, which is not generally assured by numerical optimization methods. The solution is given by:

$$(3)\ x = x_b + G(y - \hat{y})$$

where $y$ and $\hat{y}$ represent the observed and modelled concentrations, respectively, and $G$ is the gain matrix, which quantifies the sensitivity of the optimal state to the observations.

$$(4)\ G = BH^T(HBH^T + R)^{-1}$$

This project has received funding from the European Union's Horizon Europe research and innovation programme under grant agreement No 101081395

The a posteriori error covariance matrix is:

$$(5)\ A = B - BHG$$

describing the uncertainty in the posterior estimate.

## 2.2 Post-hoc non-negativity constraint

F-gases have no significant surface sinks and are removed almost entirely through atmospheric chemical processes; therefore, surface emissions are expected to be non-negative. However, because the Bayesian inversion assumes Gaussian uncertainties, negative a posteriori fluxes can occur in individual grid cells as a statistical artefact. To ensure physical consistency, a non-negativity constraint is applied to the posterior emissions using a truncated Gaussian inequality formulation, as described below.

$$(6)\ \hat{x} = x + AM^T(MAM^T + C)^{-1}(c - Mx)$$

where $\hat{x}$ denotes the constrained posterior emissions, $x$ the unconstrained posterior emission estimate, and $A$ the associated posterior error covariance matrix obtained from Eq. (5). The matrix $M$ selects the state vector elements with negative values in $x$, while the vector $c$ contains zeros corresponding to these elements. Since the non-negativity constraint is assumed to be exact, the constraint uncertainty matrix $C$ is set to zero, and the posterior error covariance matrix remains formally unchanged (Thacker, 2007).

## 2.3 Post-hoc global total constraint

For HFCs, the global emissions are assumed to be relatively well known, since they can be derived quite accurately from atmospheric growth rates, with the largest source of uncertainty being related to the rate of destruction by the hydroxyl radical (OH). The inequality-constraint framework can be adapted to impose other scalars or vectors to impose alternative constraints (e.g., global totals, regional sums). Püschel et al. (2025) first demonstrated this by constraining posterior $CF_4$ and $C_2F_6$ emissions to well-determined global totals, reducing uncertainties in poorly monitored regions. Here, we apply this concept to HFC inversions by enforcing a global-total constraint that aligns the sum of posterior HFC emissions with trusted global budgets. We refer to this approach as a post-hoc global constraint (Posterior-GC). When applying Eq. (6) as a global-total constraint in the annual HFC inversions, c denotes the estimated global-total emissions, and C denotes their associated uncertainty. Compared with the non-negativity constraint, here $M$ is an area-weighted summation operator that aggregates the entries of the posterior state vector $x$ to compare $Mx$ with the target total in $c$. For HFCs, c and C are taken from Western et al. (2025), who used the AGAGE 12-box model inversion framework (Cunnold et al., 1983; Rigby et al., 2013) to estimate global totals from background observations.

## 2.4 Inversion inputs

In atmospheric inverse modelling, the transport model, here FLEXPART v11 (Bakels et al., 2024), defines the relationship between atmospheric concentrations and emissions through sensitivity fields. These fields quantify how changes in emissions or initial conditions affect concentrations (Eq. 7). Specifically, $H_{in}$ and $H_{out}$ represents sensitivity to emissions within $(x_{in})$ and outside $(x_{out})$ the spatial domain, respectively, and $H_i$ describes sensitivity to the initial atmospheric concentration $(y_i)$.

The forward model is thus expressed as the sum of three components: contributions from emissions within the inversion domain and transport model simulation period, contributions from emissions outside the inversion domain but within the transport simulation period, and contributions from the initial mixing ratios, which account for emissions outside the transport simulation period (but could be inside or outside the inversion domain):

$$(7)\ \hat{y} = H_{in}x_{in} + H_{out}x_{out} + H_i y_i$$

This project has received funding from the European Union's Horizon Europe research and innovation programme under grant agreement No 101081395

In inversion studies, the sum of the second and third terms typically represents the background or baseline signal. The second term is only relevant for regional-scale inversions and does not apply to global inversions. The initial atmospheric concentration vector, $y_i \epsilon \mathbb{R}^k$, is often projected into a reduced space using temporal and spatial aggregation. In practice, this is done by averaging contributions within predefined latitude bands and over a specified temporal resolution, yielding a reduced vector $\tilde{y}_i \epsilon \mathbb{R}^{\tilde{k})}, where\ \tilde{k} \ll k$.

### 2.4.1 Atmospheric F-gas observations

HFC dry-air mole fractions collected between 2014 and 2023 were used for both the inversions and for nudging the initial mixing ratios towards observations. The primary datasets are from the Advanced Global Atmospheric Gases Experiment (AGAGE; (Prinn et al., 2018)) and the National Oceanic and Atmospheric Administration Global Monitoring Laboratory, LOGOS division (NOAA-ESRL-GML; (Vimont, 2015)). AGAGE provides high-frequency (hourly) surface measurements, whereas NOAA provides low-frequency (typically biweekly) surface flask samples. Following data-provider recommendations, NOAA flask observations, except for HFC-32, were converted to AGAGE calibration scales by dividing the NOAA values by the prescribed factors: to SIO-05 for HFC-134a (1.0128 for NOAA-1995-PR1 and 0.9991 for NOAA-1995), to SIO-07 for HFC-23 and HFC-143a (0.9860 for HFC-143a), and to SIO-14 for HFC-125 (0.9725). For HFC-32, AGAGE observations were converted to the NOAA scale by dividing by 1.12485.

In addition to the two major networks, we also included recently published HFC data (excluding HFC-23) from 10 Chinese flask stations; two at daily resolution and the remainder at weekly resolution, for 2014–2021 (Fang et al., 2026). Additionally, we used HFC observations from two Integrated Carbon Observation System (ICOS) stations and one China Meteorological Administration (CMA) station. The ICOS sites provide hourly data at the Taunus Observatory (TOB; excluding HFC-134a, which is available only from 2018 onward) and weekly to daily data at Cabauw Atmospheric Observatory (CBW; from 2021 onward). The Shangdianzi site (SDZ) provides hourly measurements for the period 2021–2023. All additional observations are reported on AGAGE calibration scales; therefore, no further scale conversion was applied, except for HFC-32, which was converted to the NOAA scale. Observations taken more frequently than every 3 hours were averaged to create 3-hour averages. If only one observation was available within a 3-hour period, that value was used. Flask measurements were assimilated into the inversion at their original temporal resolution.

Observation coverage is not complete for the entire 2014–2023 period at all stations. For example, in East Asia, the Gosan observatory (GSN) ceased reporting most HFCs in 2019, while HFC-23 reporting continued until 2022. At SDZ, data are available only for 2020–2021. Moreover, many station records contain gaps relative to their nominal sampling frequencies. HFC-23 is monitored only at high-frequency sites, and its emissions are largely dominated by point sources. As a result, the limited observational coverage and source characteristics make inversions for HFC-23 less robust. Most U.S. flask sites became operational in 2015, and their coverage expanded from 2016 onward. As a result, the early part of the study period is affected by limited data coverage over that region. The detailed observation availability of high-frequency and low-frequency stations is shown in Figure 2.

This project has received funding from the European Union's Horizon Europe research and innovation programme under grant agreement No 101081395

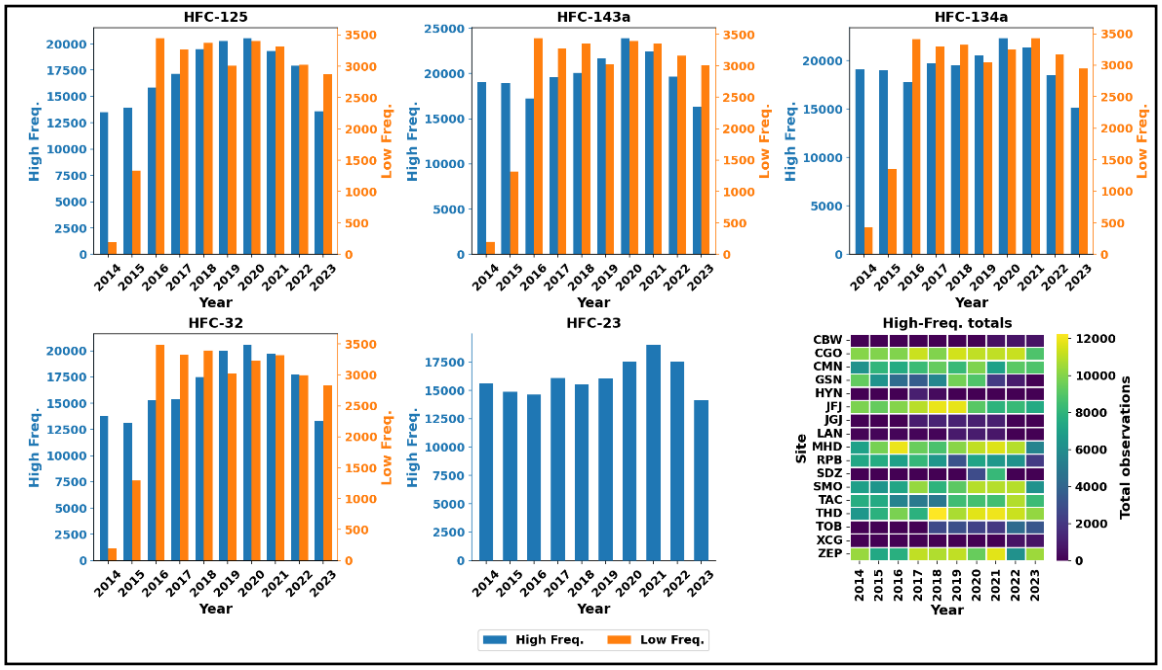


*Figure 2. Annual counts of HFC dry-air mole-fraction observations used in this study (2014–2023). Each panel corresponds to one species (HFC-125, HFC-134a, HFC-143a, HFC-32, and HFC-23). Colours distinguish high-frequency observations (daily or sub-daily) from low-frequency observations (less frequent than daily). Sub-daily data were aggregated to 3-hourly resolution prior to counting, while all other measurements were included at their native temporal resolution. Note that HFC-23 was measured only at high-frequency sites. The bottom-right panel shows the total number of HFC records available at these sites. Measurements are often intermittent; for example, GSN ceased in 2020, SDZ was available only during 2020–2021, and several stations (CBW, HYN, JG, LAN, and CGN) contain only a limited number of observations.*

Similarly, $SF_6$ dry-air mole fractions were collected during the period 2005 to 2021 and averaged to 3 hourly intervals, combining continuous online and instantaneous flask sample measurements from surface stations, with observations from moving platforms (see also Vojta et al. (2024)). Observations, provided at four different $SF_6$ scales (SIO-2005, WMO $SF_6$ X2006, WMO $SF_6$ X2014, and NIES-2008) were calibrated to the SIO-2005 calibration scale by dividing NIES-2008 calibrated data by the factor 1.013 and WMO $SF_6$ X2014 calibrated data by 1.002 (Guillevic et al., 2018). To convert mole fractions from WMO $SF_6$ X2006 to WMO $SF_6$ X2014, $y=ax^2+bx+c$ was used, where y corresponds to $SF_6$ mole fractions on the X2014 scale and x to mole fractions on the X2006 scale. The coefficients a, b, and c have the values of $2.6821\ 10^{-3}$, $9.7748\ 10^{-1}$ and $3.5831\ 10^{-2}$, respectively (NOAA-ESRL, 2014). Figure 3 shows the total number of annual $SF_6$ observations available for (a) the entire data set and (b) the averaged data set.

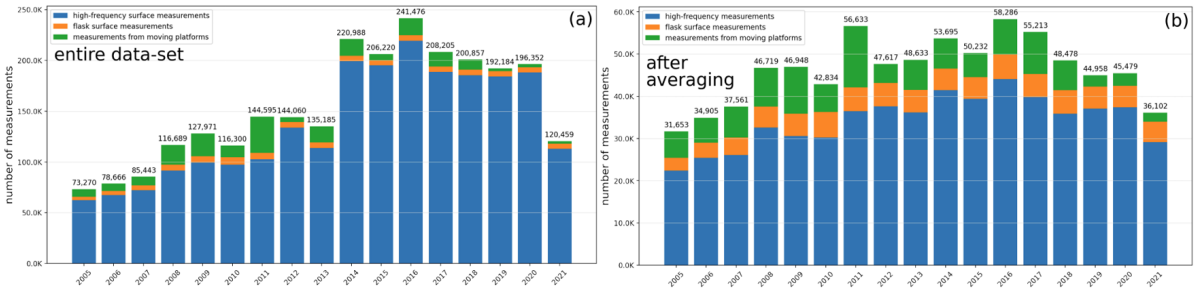


*Figure 3. The total number of annual available $SF_6$ observations of (a) the entire measurement dataset and (b) the dataset after averaging. The different colours indicate the different measurement types; blue: continuous, high-frequency surface measurements; orange: flask surface measurements; green: measurements from moving platforms.*

This project has received funding from the European Union's Horizon Europe research and innovation programme under grant agreement No 101081395

### 2.4.2 Sensitivity fields

The sensitivity fields ($H_{in}$ and $H_{out}$), referred to as the source-receptor relationships (SRRs), were produced using the Lagrangian Particle Dispersion Model (LPDM) FLEXPART v11 (Bakels et al., 2024) in backward-in-time mode. For each 3-hour measurement interval, 50,000 virtual particles were released from observation sites and traced backward for 50 days. A 50-day simulation period was selected, based on (Vojta et al., 2022) demonstrating that this longer back trajectory periods enhance inversion accuracy, compared to shorter ones (comparing to 1, 5, 10, 20 days). FLEXPART was driven by ERA5 meteorological reanalysis data (Hersbach et al., 2020) at 0.5° × 0.5° horizontal resolution and 137 vertical levels. FLEXPART was configured to compute SRRs ($sm^3\ kg^{-1}$) for each grid cell in the lowest 100 m, assuming only near-surface emissions of F-gases. SRRs were computed at 1°×1° globally and 0.5°×0.5° for the European regional domain (30°W–40°E, 30°N–80°N). OH-driven chemical loss, the main sink for HFCs, is negligible over the 50-day backward period. Therefore, HFCs were treated as inert when constructing the sensitivity fields, which simplifies the workflow without introducing significant error (<3% for HFC-32 and <1% for the others). Loss processes can also be neglected for $SF_6$, as it is almost inert up to the middle stratosphere. Emission sensitivities are highest near measurement sites and gradually decrease with distance. It is worth noting that both $H_{in}$ and $H_{out}$ are derived from the same calculations and are simply masked based on the inversion domain. Figure 4 shows the 2019 annual total 50-day surface SRR field for stations measuring HFCs. SRRs were computed for all timestamps with at least one available HFC observation. An analogous analysis for $SF_6$ is provided in Vojta et al. (2024). In the regional inversions (for Europe), SRRs inside the purple rectangle are assigned to $H_{in}$, and SRRs outside to $H_{out}$. Representing collected timestamps for all studied F-gases in 2019, these SRRs are unlikely to effectively constrain many regions. This is evident even in relatively better-observed regions such as the United States and Europe, and it is more pronounced in regions like South America, Africa, India, and the Middle East, where total SRRs are close to zero. These near-zero values indicate very weak or no observational constraint, underscoring a severe data-coverage limitation for F-gas inversions. Furthermore, HFC-23 is not measured at low-frequency stations, so SRRs from those sites, often available for other HFCs, particularly at higher latitudes and in the eastern United States, do not contribute to the HFC-23 inversion, further exacerbating the coverage gap. The station markers overlaid on the SRR field are primarily illustrative, reflecting activity for most, but not all, stations across the entire study period. For example, observations from the only station in China monitoring HFCs (SDZ) are available only in 2020–2021; thus, the 2019 SRRs near that location correspond to the Gosan station in Korea. For detailed information on station activity, see Figures 2 and 3.

The sensitivity to the initial condition ($H_i$) is another standard output of FLEXPART (not shown here), defined as the fraction of the number of trajectories terminating in a specific grid cell divided by the total number of virtual particles released, assuming no loss processes. The initial sensitivities of each 50-day backward simulation are stored on a 1° × 1° grid across 12 vertical levels, with upper boundaries at 0.1, 0.5, 1, 2, 3, 5, 7, 9, 12, 15, 20, and 50 km. Initial mixing ratios are subsequently calculated by spatially integrating the product of these sensitivities and the global 3D gridded mole fractions, which are described in subsection 2.4.4.

This project has received funding from the European Union's Horizon Europe research and innovation programme under grant agreement No 101081395

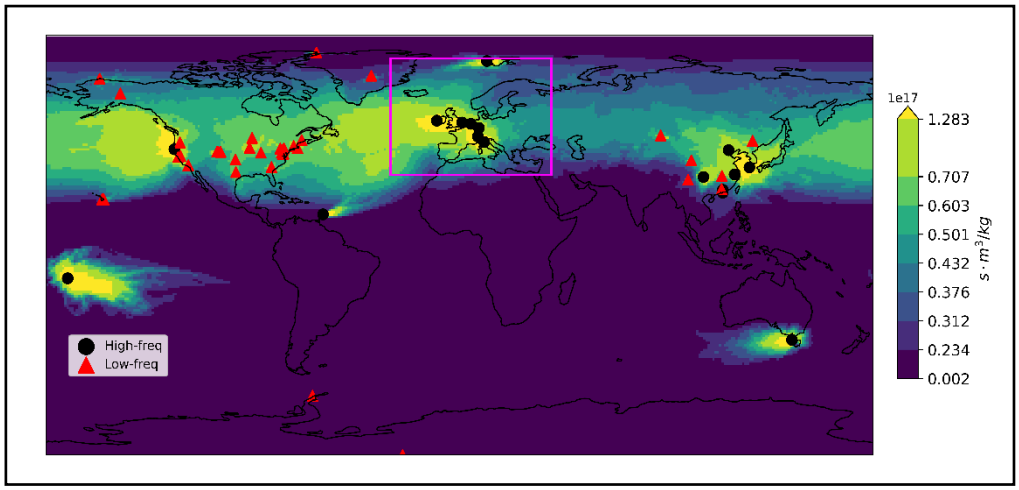


*Figure 4. Annual total of 50-day source-receptor relationship SRRs obtained with FLEXPART backward runs for the sample year 2019. Dots and rectangles are respectively showing the location of high-frequency HFC observations (daily or sub-daily) and low-frequency HFC observations (less frequent than daily). Higher values of SRRs indicate regions well constrained by the observational network. The Northern Hemisphere shows high sensitivities, particularly in North America, East Asia, and Europe, whereas the Southern Hemisphere is much less constrained. The purple box indicates the European inversion domain.*

### 2.4.3 A priori emissions

We constructed HFC a priori emissions using two spatially resolved, global bottom-up inventories: (1) GAINS (Purohit and Höglund-Isaksson, 2017), (2) EDGAR release 2024 (EDGAR; (Crippa et al., 2023)). Assuming that the global totals inferred from observations by the AGAGE 12-box model (Western et al., 2025) provide the most reliable estimates, we scaled both inventories to match these totals at the global level. Hereafter, GAINS and EDGAR refer to the scaled inventories, while the unscaled versions are denoted as "GAINS-unscaled" and "EDGAR-unscaled" where applicable. GAINS and EDGAR are available at a native spatial resolution of 0.1°. Both inventories were regridded to the inversion grids: 1° × 1° for the global inversions and 0.5° × 0.5° for the regional inversion.

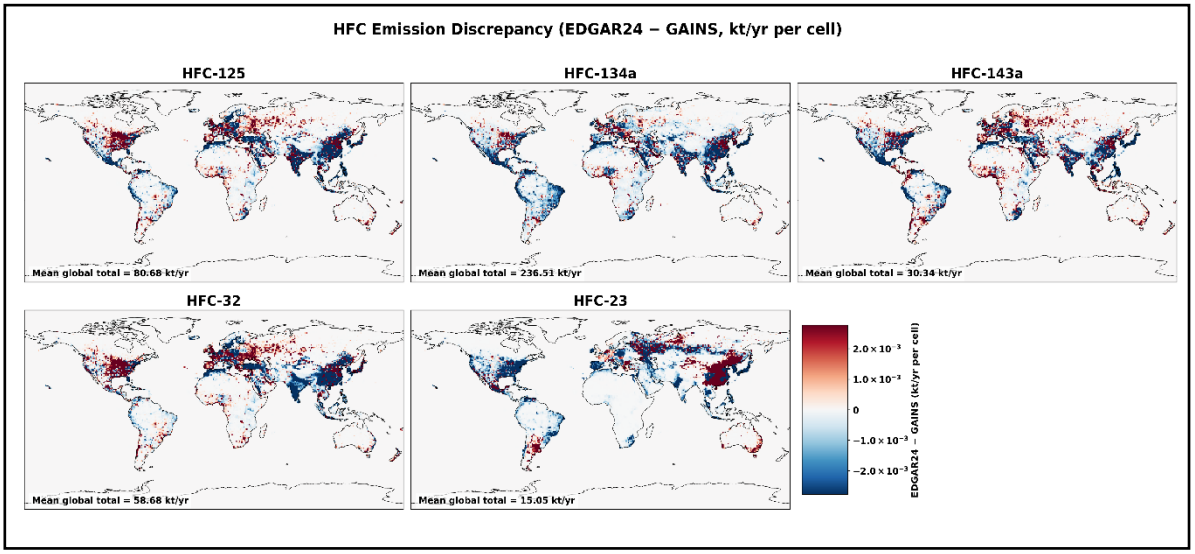


*Figure 5. Spatial discrepancy between prior HFC emissions from EDGAR and GAINS, shown as EDGAR − GAINS (kt yr⁻¹ per grid cell) averaged over 2014–2023 for five species (HFC-32, -125, -134a, -143a, -23). Red indicates EDGAR > GAINS, and blue indicates the opposite.*

The spatial distribution of HFC emissions points to a Northern Hemisphere belt, with major source regions located in East Asia, India, the Middle East, Europe, and the eastern United States (Fig. 5).

This project has received funding from the European Union's Horizon Europe research and innovation programme under grant agreement No 101081395

EDGAR tends to be higher over Eastern Europe, Russia, and the coastal/eastern China corridor, whereas GAINS is often higher over mid- and western China, India, the Middle East, and South America. The sign and intensity of the differences vary substantially across HFCs, particularly over central and western Europe and the eastern United States. For HFC-125, Europe and the United States are characterized by higher emission levels in EDGAR, while GAINS shows higher emissions across the other major emitting regions. For HFC-134a, higher GAINS emissions are more broadly distributed across source regions, especially over eastern China. A similar pattern is observed for HFC-143a, with more frequent EDGAR hotspots over northeastern Europe, Russia, Africa, and South America. For HFC-32, EDGAR clearly exceeds GAINS across the eastern United States and most of Europe, whereas GAINS is higher in the remaining major emitting regions. The strongest differences are found for HFC-23: EDGAR-GAINS shows pronounced positive differences centered over eastern China, with additional signals over Eastern Europe and Russia, as well as a major hotspot in Argentina and Uruguay, whereas GAINS estimates are higher over central Russia, most of Europe, and across the majority of emission regions in the United States. The more limited spatial extent of emissions for HFC-23, along with the dominant contribution from China, is also evident. Overall, EDGAR tends to exhibit stronger localized enhancements, while GAINS generally shows a more spatially distributed emission pattern, with systematic regional differences between the two inventories.

For $SF_6$, a priori emissions were also based on EDGAR, GAINS and the UNFCCC reports (UNFCCC-ELE). For the latter, we gathered total national $SF_6$ emissions reported to the UNFCCC and added total Chinese emissions estimated by Fang et al. (2014). We then subtracted the total emissions of these countries from the total global $SF_6$ emissions calculated by Simmonds et al. (2020). The residual emissions are then distributed among all other countries proportionally to their national electricity generation. Lastly, the attributed total national $SF_6$ emissions were further distributed within the respective borders of each country according to gridded population density and night light remote sensing data (see Vojta et al. (2024)). Figure 6 shows significantly higher emissions in the Northern Hemisphere than in the Southern Hemisphere for all three fields, with China being the biggest emitter. Other high-emitting areas are Europe, the USA, and India. While emissions in Europe are comparable across all data sets, notable differences can be seen in other regions: UNFCCC-ELE shows relatively high emissions in India and the Southern Hemisphere compared to EDGAR and GAINS, EDGAR shows higher emissions in the USA than the other two a priori fields, and GAINS exhibits higher emissions in China than UNFCCC-ELE and EDGAR.

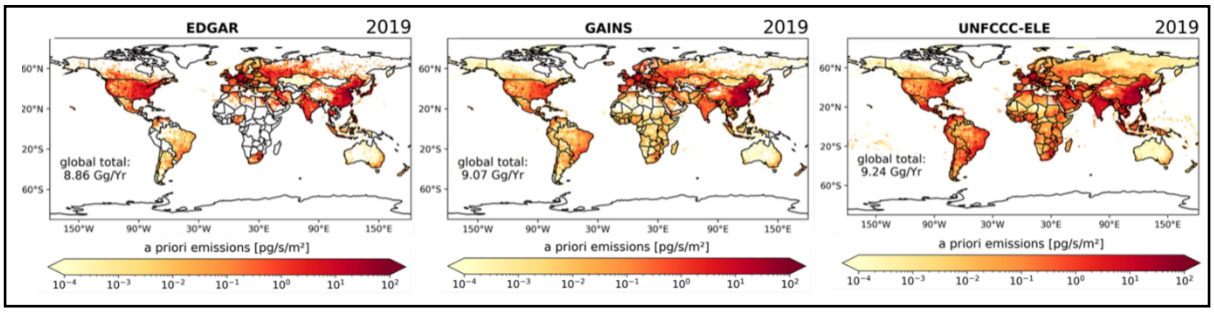


*Figure 6. A priori emissions based on three different sources: EDGAR, GAINS, and UNFCCC-ELE, shown for the year 2019.*

### 2.4.4 Initial mixing ratios

Because there is no publicly available global reanalysis of F-gas mixing ratios, we produced our own global reanalysis to supply initial mixing ratios for this study. For the HFCs, we ran the FLEXPART Linear Chemistry Module (FLEXPART-LCM; Bakels et al. (2024)) in a forward, domain-filling configuration.

This project has received funding from the European Union's Horizon Europe research and innovation programme under grant agreement No 101081395

FLEXPART-LCM is derived from the FLEXPART chemical transport model (FLEXPART-CTM), which we also used for $SF_6$ (Vojta et al., 2024) and which was originally developed by Henne et al. (2018) and described by Groot Zwaaftink et al. (2018). We largely adopted the FLEXPART-LCM setup from the 3D global $SF_6$ reanalysis in Vojta et al. (2024).

We released 50 million particles globally, each carrying an air tracer and the chemical species. Daily mixing-ratio fields were archived on a 3° × 2° grid with 10 vertical levels whose upper boundaries are 0.1, 0.5, 1, 3, 5, 7, 10, 15, 25, and 40 km above ground. This reduced output resolution was chosen to limit storage requirements, as higher-resolution output has been found to have only a negligible impact on the inversion results. This is because, in our 50-day backward-trajectory setup, the posterior emission estimates are primarily constrained by the source–receptor relationships (SRRs), which are calculated at the native FLEXPART model resolution of 1° globally and 0.5° over the regional domain. To shorten spin-up, particle masses were initialized from a latitudinal mixing-ratio profile interpolated from background observations within a ±60-day window around the start date. A single continuous simulation was not practical, so we split the period into yearly segments run in parallel, each re-initialized and preceded by a six-month spin-up. During the simulation, FLEXPART-LCM does not release new particles; instead, it increments the masses of particles that traverse emitting grid cells in source regions.

To reduce baseline errors arising from both emissions and transport, we applied a simple nudging scheme that steers modelled mixing ratios toward observations when particles pass within predefined spatio-temporal kernels around measurement sites, following Groot Zwaaftink et al. (2018). The nudging dataset matches the observations used in the inversion (defined above). While nudging improves large-scale backgrounds, it cannot fully correct regional biases given the sparse HFC coverage, particularly for HFC-23.

Emissions for the long-term FP-LCM baseline are based on EDGAR. However, since the test runs and nudging parameter tuning were completed before the release of EDGAR, EDGAR v8 was used instead. Both EDGAR v8 and the unscaled inventories (GAINS and EDGAR) show noticeable biases in global totals compared to AGAGE 12-box estimates. As a result, some residual bias in the simulated background is expected even after nudging during the parameter tuning runs (shown in Figure 7). The impact of the nudging on background HFC simulations for March–May 2018 is illustrated at validation stations (NWR, CMN, ALT, INX, TAC) that were excluded from the nudging. HFC-23 is not evaluated due to an insufficient number of stations for removing some of them for validation. Overall, nudging yields systematic improvements: errors decrease, correlations increase, and mean biases move toward zero. Nevertheless, species-dependent residual biases remain, negative for HFC-125 and HFC-134a, positive for HFC-143a and HFC-32. For HFC-125, the negative bias becomes larger after nudging. The largest discrepancies occur at the mountainous CMN site, likely reflecting a combination of terrain elevation mismatches between the model and reality, boundary-layer variability, and uncertainties in nearby emissions. The coarse resolution of FLEXPART-LCM output and the relatively low number of particles (50 million) can lead to large representation and statistical errors when comparing to point measurements. For the inversion, these errors are less relevant because initial conditions at the termination points of the Lagrangian backward simulations are sampled from a large atmospheric volume, typically covering many hundreds of grid cells.

This project has received funding from the European Union's Horizon Europe research and innovation programme under grant agreement No 101081395

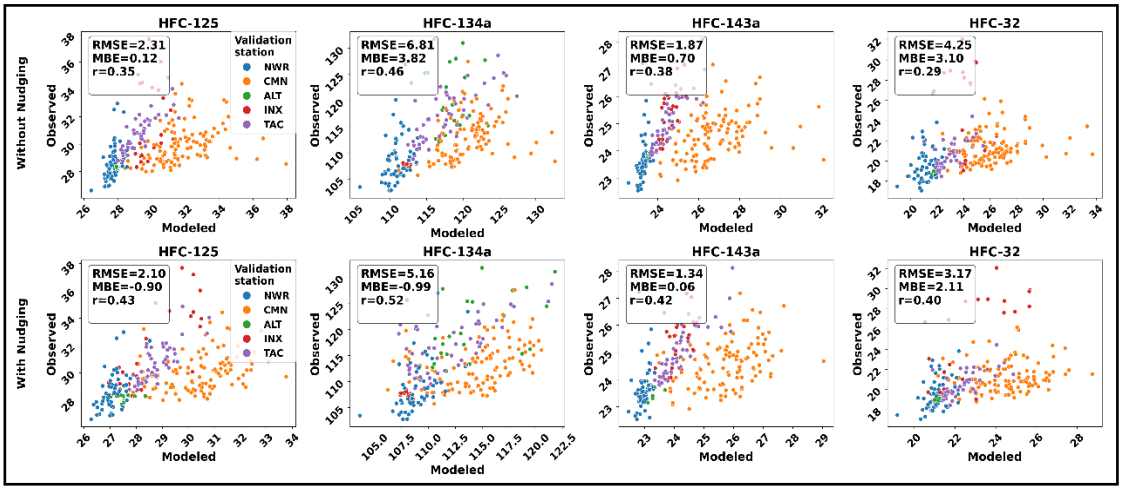


*Figure 7. Scatter plots of observed vs. modelled concentrations for each element (column) and nudging experiment (row) over the period 2018-03-01 to 2018-06-28. Points are coloured by validation station. Each panel reports performance metrics: MSE, RMSE, MBE, and Pearson correlation r. Axes are observed concentration (y) and modelled concentration (x).*

### 2.4.5 Uncertainty assessment

Accurately quantifying uncertainties in optimized emissions is a key challenge in inverse modelling and is discussed in greater detail elsewhere (see Project Task 3.8). Traditionally, the uncertainties in inversion-derived emissions are based on Gaussian error statistics within a Bayesian framework, often relying on a single inversion setup. However, many aspects of the inversion process are based on assumptions and expert judgments. Several studies (e.g., Bergamaschi et al. (2015); Brunner et al. (2017); Chevallier et al. (2019); Locatelli et al. (2013)) have demonstrated that the range of emissions derived from different inversion configurations can be significantly larger than the uncertainties calculated by individual inversions. Therefore, Vojta et al. (2025) examined the sensitivity of the $SF_6$ inversion results to various inversion settings by systematically varying key parameters starting from a reference inversion. While the sensitivity studies provide insight into how different parameter settings influence the inversion results, the overall uncertainties of the inversion are determined by all these parameters simultaneously. Therefore, to accurately quantify the inversion uncertainties, one must apply random variations of these parameters. However, testing all possible combinations is infeasible due to the vast number of permutations. For European $SF_6$ inversions we employ a Monte Carlo method to randomly select and combine inversion parameters, creating inversion ensembles. For the HFCs, the sampling across the parameter space was performed using Latin Hypercube Sampling (LHS) (Helton and Davis, 2003). LHS is a stratified, space-filling variant of Monte Carlo sampling that partitions each parameter's cumulative distribution function (CDF) into N intervals of equal probability, from which one value is randomly drawn (Lucas et al., 2017). This approach ensures a more uniform exploration of each parameter's range than conventional Monte Carlo (MC) sampling and, consequently, requires fewer samples to achieve comparable precision in uncertainty estimates. Our inversion ensemble spanned combinations of (i) priori emission inventories, (ii) prior- and observation-error parameters, (iii) initial mixing ratio uncertainty and the number of latitude bands used to optimize initial mixing ratios , and (iv) the resolution of the state vector. Specifically:

- Priori emission inventories were treated as a categorical choice between GAINS and EDGAR to reflect structural uncertainty in source magnitudes and spatial patterns.

- The prior error covariance matrix $B$ was varied in its spatial correlation length scales, overall flux-uncertainty amplitude, and a minimum uncertainty floor.

- For the observation error covariance $R$, we investigated four different approaches: uncertainty linearly scaled with the prior mixing ratio (Katharopoulos et al., 2023); pollution-event–scaled uncertainty

This project has received funding from the European Union's Horizon Europe research and innovation programme under grant agreement No 101081395

(Ganesan et al., 2025); site-specific RMSE derived from prior simulations (Vojta et al., 2025); and a fixed uncertainty sampled from an assumed Gaussian distribution.

- To test sensitivity to model errors in complex terrain, we used a binary switch in the ensemble to include or exclude mountain sites (altitude >1000 m a.s.l.). This impacts 11 out of 56 stations studied through the study period.

- The impact of state vector resolution (through grid coarsening/refinement) was assessed using two inversion-domain resolutions, computed annually for each species and inversion domain (global and regional): a high-resolution case (~6700 grid points, e.g. for 2018 HFC-134a in the global domain) and a low-resolution case (~4670 grid points for the same year and species in the global domain).

- Sensitivity to boundary/initial-condition specification and the latitude-gradient resolution was examined by adjusting the initial mixing ratio uncertainty and the number of latitude bands employed in the initial mixing ratio optimization.

Continuous parameters, such as prior uncertainties or initial mixing ratio error, were sampled from underlying Gaussian distributions as to focus on the most probable value (mean of distribution). The mean was decided by pilot sensitivity inversions, expert judgment, and prior studies (Brunner et al., 2017). The standard deviation was set to $\sigma$=0.5 $\mu$ (a coefficient of variation of 0.5) to allow broad exploration of parameter space. We treated categorical parameters (inventory choice, observational error scheme, grid resolution) with uniform discrete sampling assuming no strong prior preference existed among categories. We used approximately 1000 samples to balance computational cost with a comprehensive coverage of influential parameter combinations. Figure 8 summarizes the underlying distributions from which samples were drawn for all continuous parameters and, as one categorical example, the emission inventories. As with the emission inventory, other categorical/discrete parameters, including the number of latitude bands used for optimization, inversion-domain resolution, mountainous-site selection (binary), and the measurement-uncertainty approach, were sampled independently under a uniform prior (equal probability for each category; not shown here). The measurement-uncertainty distribution shown in Figure 8 is in fact the result of assuming a fixed uncertainty for all observations, one of the four methods used to assign observation uncertainties in the inversions. In this approach, the mean and spread of the underlying Gaussian distribution are derived from the results of the other three methods. The distributions for measurement uncertainty, initial mixing ratio uncertainty, and lower bounds on prior flux uncertainties (which vary with inventories) are updated every year and for each species. The parameter distributions shown here are specifically for the year 2018 and for the species HFC-134a.

This project has received funding from the European Union's Horizon Europe research and innovation programme under grant agreement No 101081395

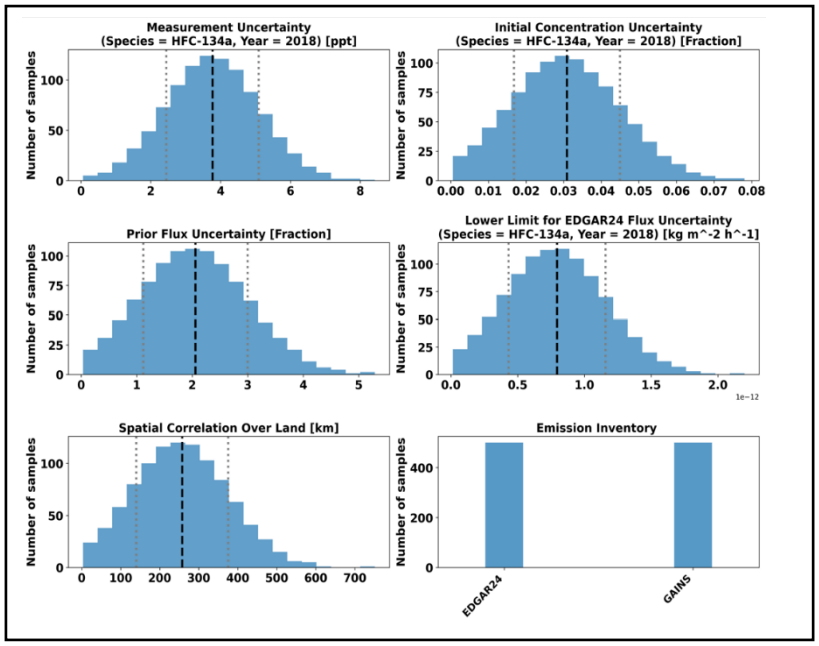


*Figure 8. Assumed parameter distributions used for ensemble sampling for HFC-134a in 2018. Panels show continuous variables, measurement uncertainty (ppt), initial-concentration uncertainty (fraction), prior uncertainty (fraction), lower limit for EDGAR flux uncertainty (kg m−2 h−1; shown as an example, with analogous inputs produced for GAINS), and spatial correlation length over land (km), and one categorical parameter: the emission inventory (EDGAR and GAINS). The x-axis shows parameter values (or categories), and the y-axis shows the number of samples in each bin or category across 1000 runs. Other categorical parameter, including latitude-band count, inversion-domain resolution, mountainous-site selection (binary), and measurement-uncertainty approach (four categories), were sampled under a uniform prior (equal probability; not shown). For continuous parameters, the vertical dashed line marks the mean and the dotted lines indicate the 1$\sigma$ range. Distributions are updated annually and by species.*

# 3. Results

For reporting the inversion results, we focus on regions that are well constrained by the observing network and do not interpret outcomes for poorly sampled areas (West Asia, India, Russia, Africa, and South America; Fig. 4). In the Supplement, we illustrate how sparse coverage affects emission uncertainty reduction, defined as (1 − σpost/σprior) × 100. Here, we first present diagnostics in observation space, followed by posterior emissions for China and the United States from the global inversion, and for Europe from the regional inversion, along with major emitting countries such as the UK, Germany, and France.

## 3.1 Inversion performance in observation space

The impact of the inversion in observation space was evaluated using a representative ensemble member, defined as the member whose country emission totals are closest to the ensemble median in terms of Euclidean distance. MBE (Fig. 9), RMSE (Fig. S4), and Spearman correlation (Fig. S5) were then computed between prior and posterior concentrations and the observations, with correlations derived from detrended time series so that the metric reflects agreement in temporal variability rather than shared long-term trends. These metrics were evaluated across measurement sites for the period 2015–2021, which provides the highest observational coverage. Overall, the inversion results in improved agreement between modelled and observed concentrations, with consistent performance gains across all evaluated metrics. MBE for selected stations is shown in Fig. 9, while results for the full list of stations are presented in Fig. S3. Background sites (e.g., ZEP, MHD, RPB) show generally good agreement both before and after inversion, reflecting their remoteness from major emission regions and the dominant contribution of initial mixing ratios . At these locations, the measurements provide only

This project has received funding from the European Union's Horizon Europe research and innovation programme under grant agreement No 101081395

weak constraints on the emissions. Posterior biases are generally smaller than prior biases, indicating a successful reduction in systematic error. The only exception is GSN for HFC-32, where MBE increases after inversion, despite concurrent improvements in RMSE and correlation. Except for HFC-32, the HFC priors are generally negatively biased, suggesting a likely systematic underestimation of emissions in major source regions. A clear deviation, characterized by a large positive MBE, is observed at SDZ (China; shown in Fig. S3). The largest reduction of MBE also occurs at SDZ, pointing to an overestimation of most HFC emissions in China, as discussed further below. Larger residual posterior biases, i.e., remaining biases after inversion despite clear reductions relative to the prior, persist at sites such as INX and TOB across all HFCs. At TOB, this likely reflects substantial priori emission errors, compounded by proximity to emission sources and transport-related uncertainty. At INX, similar factors apply, further exacerbated by the limited number of available observations. Despite overall improvements in RMSE and correlation (Figs. S4 and S5), the modest gains likely reflect the coarse resolution of SRRs, which limits the representation of sharp concentration gradients and increases model errors and representation errors close to sources. This effect is further amplified by unresolved local sources in the prior inventories and the spatial correlation (smoothing) assumptions in the inversion, which tend to favor regional consistency over local-scale adjustments. Among species, HFC-23 exhibits the weakest Spearman correlation (both prior and posterior) at a limited number of high-frequency measurement sites. This likely stems from the difficulty of representing spatially and temporally heterogeneous local HFC-23 emissions within the current inversion framework, as well as data scarcity. It is worth noting that the performance metrics at European sites are comparable between the regional (not shown here) and global inversions.

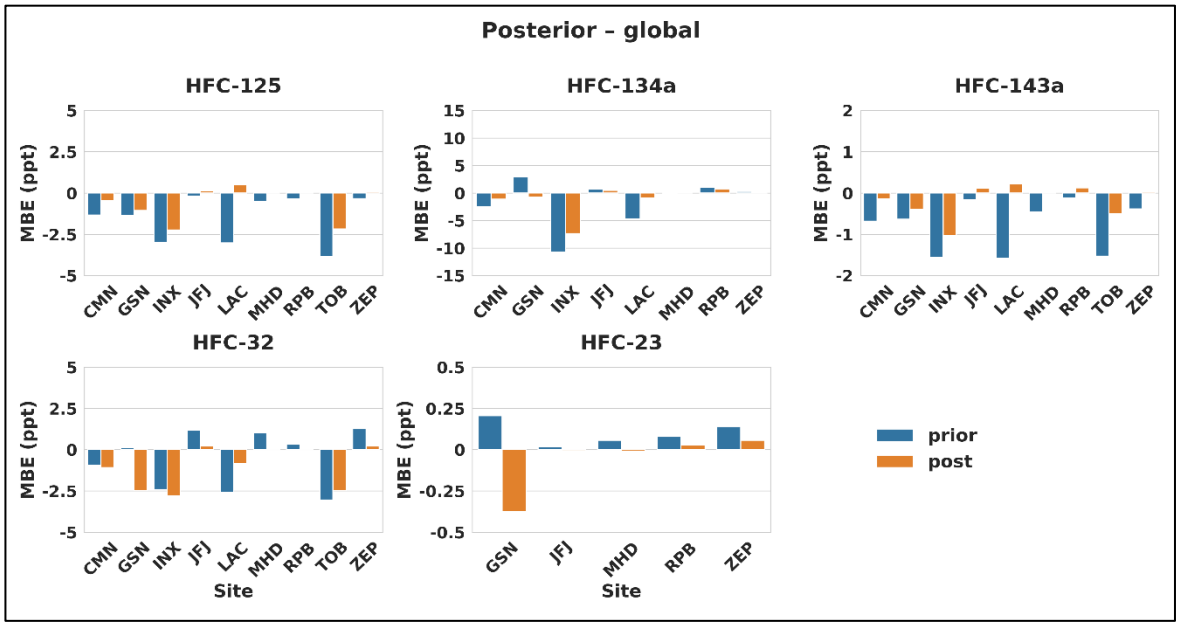


*Figure 9. MBE before and after inversion for the selected stations (full list in the Supplement), shown for a representative inversion ensemble member selected by proximity to ensemble median country totals, for the period 2015 and 2021 with largest observations coverage. Corresponding results for RMSE and Spearman correlation for all sites are presented in Supplementary Figures S3 and S4.*

## 3.2 Emissions estimated in major source regions

Before presenting the posterior estimates, we note that data availability for HFCs varies across regions, with some gaps in the most recent years. To ensure a consistent comparison across China, the US, and Europe, we focus on the period 2015–2021, which provides sufficient observational coverage for all regions. To obtain a more robust analysis of emission growth rates and mean posterior adjustments relative to the prior, estimates from 2015–2016 and 2020–2021 were considered. The reported emission

This project has received funding from the European Union's Horizon Europe research and innovation programme under grant agreement No 101081395

values represent medians, and the error ranges reflect the 5th and 95th percentiles of the ensemble estimates. For the global $SF_6$ inversions, available from 2005 to 2021 in all regions, uncertainties are defined as the minimum and maximum 1σ uncertainty limits across inversion results obtained using different a priori assumptions, as described in Vojta et al. (2024).

### China

Over the period from 2015–2016 to 2020–2021, China's total $CO_2$-equivalent emissions of the five studied HFCs show a clear increase, rising from 273.0 (166.1–362.2) to 323.8 (231.6–397.9) Tg $CO_2$-eq $yr^{-1}$. This corresponds to a median rise of 50.7 Tg (+18.6%) across the two analysis windows. At the species level, the most pronounced change is seen in HFC-32, which shows a strong increase of +86.7% in the posterior estimates between the two periods. In contrast, HFC-143a stands out as the only species with a declining trend in China, decreasing by −2.3%, while the remaining species show moderate increases. In the context of the Kigali Amendment to the Montreal Protocol, the phasedown of high-GWP refrigerants has accelerated the transition toward lower-GWP alternatives, including HFC-32–based systems. As China is a major hub for both the production and consumption of cooling technologies, this transition is likely a key driver of the observed increase in HFC-32 emissions.

While both the prior (defined as the mean of GAINS and EDGAR estimates) and posterior indicate a consistent upward trend across most species, with the exception of HFC-143a, the prior suggests substantially stronger growth than inferred by the inversion. The prior rises from 311.8 to 412.3 Tg $CO_2$-eq $yr^{-1}$, corresponding to a median gain of 100.5 Tg (+32.2%). This pattern is also reflected at the species level. For HFC-32, the prior suggests a very strong increase (+123.5%), whereas the posterior indicates a more moderate rise (+86.7%). Similarly, HFC-134a and HFC-125 show systematically weaker growth in the posterior than in the prior. HFC-143a is particularly notable, as the posterior indicates a decline (−2.3%), whereas the prior suggests a slight increase (+3.7%).

Looking at the relative differences between posterior and prior estimates further reinforces this pattern. Across all five HFC species, posterior emissions are consistently lower than the prior, with mean relative differences of approximately −38.0% for HFC-32, −31.3% for HFC-134a, −22.5% for HFC-125, −12.4% for HFC-143a, and −7.3% for HFC-23. Overall, these results indicate that the inversion consistently moderates both the magnitude and the growth rate of emissions relative to the prior in China. A full summary of these results is provided in Table 1.

*Table 1. Posterior and prior HFC emissions in China for the periods 2015–2016 and 2020–2021, their absolute and relative changes, and posterior–prior differences are shown for each species and total $CO_2$-eq emissions.*

| Species / Metric | Posterior (kt $yr^{-1}$) 2015-2016 | Posterior (kt $yr^{-1}$) 2020-2021 | Posterior Relative Change | Prior (kt $yr^{-1}$) 2015-2016 | Prior (kt $yr^{-1}$) 2020-2021 | Prior Relative Change | Posterior vs Prior (Mean Relative Difference) |
|---|---|---|---|---|---|---|---|
| **HFC-125** | 13.1 (9.2–17.8) | 17.9 (14.2–20.5) | 36.6% | 14.6 | 25.5 | 74.8% | -22.5% |
| **HFC-134a** | 29.0 (23.8–34.7) | 36.4 (31.5–47.2) | 25.3% | 38.4 | 52 | 35.5% | -31.3% |
| **HFC-143a** | 3.6 (2.4–5.6) | 3.5 (3.1–4.1) | -2.3% | 3.8 | 3.9 | 3.7% | -12.4% |
| **HFC-32** | 12.3 (8.8–16.3) | 23.1 (18.5–27.5) | 87.6% | 18.2 | 40.7 | 123.5% | -38% |

This project has received funding from the European Union's Horizon Europe research and innovation programme under grant agreement No 101081395

| | | | | | | | |
|---|---|---|---|---|---|---|---|
| **HFC-23** | 10.2 (5.1–13.5) | 11.2 (6.7–14) | 9.3% | 11.1 | 12.6 | 12.8% | -7.3% |
| **Total $CO_2$-eq Emissions (Tg $CO_2$-eq $yr^{-1}$)** | 273 (166.1–362.2) | 323.8 (231.6–397.9) | 18.6% | 311.8 | 412.3 | 32.2% | — |

Global constraints have only a limited effect on the Posterior-GC estimates, which generally remain close to the unconstrained posterior values (Posterior). The only noticeable impact is observed during 2022–2023, when observations from eastern Asia are unavailable, increasing the influence of the global constraint on the inversion solution (Fig. 10). During this period, the unconstrained estimates exhibit abrupt variations, most notably for HFC-23. While the global constraint slightly moderates these fluctuations, noticeable discontinuities remain in the constrained estimates.

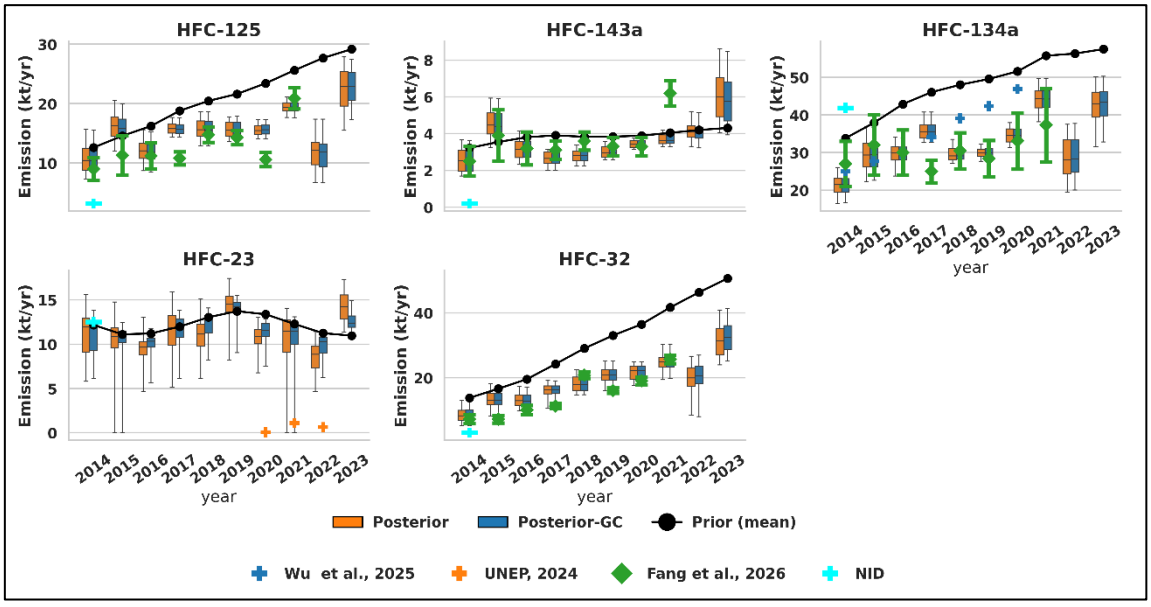


*Figure 10. China's annual emissions (kt $yr^{-1}$) for five HFC species (HFC-125, HFC-143A, HFC-134A, HFC-23, HFC-32) from 2014–2023. Boxplots show posterior ensembles for unconstrained Posterior (orange) and constrained Posterior-GC (navy), with whiskers indicating the 5–95th percentile range. The black line shows the prior mean computed from EDGAR and GAINS. Colored markers denote literature estimates with uncertainties (Wu et al., 2025; UNEP, 2024; Fang et al., 2026), where TD inventories are plotted as diamonds and BU inventories as crosses.*

Figure S6 illustrates that posterior estimates of HFC-23 emissions in China are highly sensitive to the choice of prior inventory, whereas the remaining HFC species exhibit only limited sensitivity. In particular, posterior HFC-23 emissions derived using the GAINS prior are systematically lower than those obtained using the EDGAR inventory. This behaviour likely reflects differences in the assumed spatial distribution of emissions between the inventories. Because HFC-23 emissions are typically dominated by a relatively small number of localized industrial sources, discrepancies in spatial allocation can strongly influence the inversion outcome. In contrast, species with more spatially distributed emission patterns appear substantially less sensitive to the choice of prior inventory.

Previous top-down (TD) estimates by Fang et al. (2026), extending the work of Yao et al. (2019), quantified HFC emissions in China using observations from 10 stations, which are also used in the present study. Excluding HFC-23, which was not included in their inversion framework, our posterior

This project has received funding from the European Union's Horizon Europe research and innovation programme under grant agreement No 101081395

estimates generally agree well with those reported by Fang et al. (2026), despite methodological differences such as their substantially larger prior uncertainties (up to 500 %, compared to a mean uncertainty of approximately 250 % in this study) and differences in baseline treatment, with Fang et al. (2026) applying the method of Stohl et al. (2009). Nevertheless, they reported lower estimates for some individual years, most notably for HFC-134a in 2017 and HFC-125 in 2020, for which our posterior estimates are approximately 40 % and 50 % higher, respectively.

Independent bottom-up (BU) estimates available during the study period remain relatively limited. Publicly available datasets include the national inventory dataset (NID) reported to the UNFCCC for 2014, covering all investigated HFCs together, as well as species-specific estimates for HFC-23 from UNEP (2024) and for HFC-134a from Wu et al. (2025). The NID estimates suggest lower emissions for HFC-32, HFC-143a, and HFC-125 than both the prior and posterior estimates derived in this study, whereas HFC-134a emissions reported by the NID are comparatively higher than the other available estimates. For HFC-23, our 2014 estimates agree well with the NID values. Our posterior estimates for 2020–2022 (7–12 kt $yr^{-1}$) are substantially higher than the near-zero UNEP BU estimates. This discrepancy suggests the presence of emissions that may not be captured within the UNEP bottom-up accounting framework. Independent TD estimates for eastern China reported by Park et al. (2023), indicating emissions of approximately 5–9 kt $yr^{-1}$ during 2014–2019, further support this interpretation. For HFC-134a, our posterior estimates agree well with the BU estimates of Wu et al. (2025) during 2014–2016. After 2016, however, our estimates remain approximately 30–40 % lower than the BU values and show a smoother increase toward 2020.

China also represents the largest global source of $SF_6$, accounting for approximately half of worldwide emissions. The inversion-derived Chinese a posteriori emissions (Fig.11) reveal a distinct positive trend of 0.21 kt yr−1, growing from 1.28 (1.03–1.57) kt in 2005 to 5.16 (84.75–5.60) kt in 2021, with a particularly rapid increase between 2006 and 2014 (0.35 kt yr−1), followed by a stabilisation thereafter. This stabilization coincides with Chinese regulations implemented in 2012 (GB/T-28537-2012) and 2015 (GB/T-32151.2-2015), setting standards for using $SF_6$ in high-voltage switch gear, specifying the installation, maintenance, and disposal of the equipment. Our results align closely with the inversion study by An et al. (2024) (agreeing within 12 %), who had access to data from a relatively dense monitoring network over China. China is not obliged to report its national emissions, but it voluntarily reported bottom-up $SF_6$ estimates in their national communications and biennial updates to the UNFCCC for 2005, 2010, 2012, 2014, 2017, and 2018. These reported values are much smaller than our a posteriori emission, especially in 2010, 2012, and 2014. The values from the more recent reports in 2017 and 2018 are, however, closer to our inversion results, indicating an improvement in Chinese reports (see Vojta et al. (2024)).

This project has received funding from the European Union's Horizon Europe research and innovation programme under grant agreement No 101081395

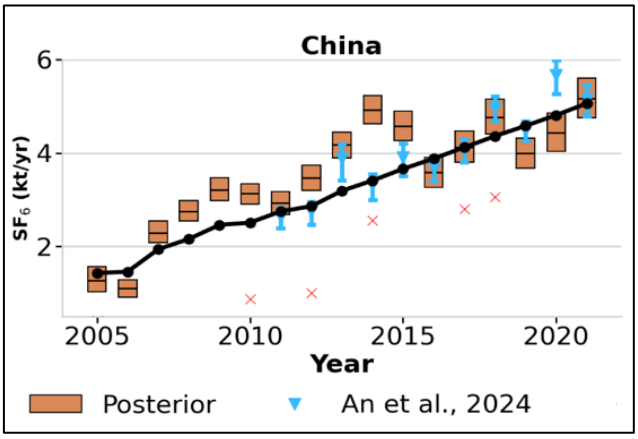


*Figure 11. Annual a posteriori $SF_6$ emissions (orange boxes) for China shown for the period between 2005 and 2021, together with their respective uncertainties. Coloured triangles represent estimated values from An et al, (2024, light blue) and black dots show the prior averaged over different inventories, while red crosses represent reported values to UNFCCC (NID).*

## USA

Over 2015–2016 to 2020–2021, total U.S. $CO_2$-equivalent HFC emissions show a substantial increase, rising from 170.7 (136.4–203.8) to 212.8 (184.3–236.3) Tg $CO_2$-eq $yr^{-1}$, corresponding to a median rise of 42.0 Tg (+24.6%). This growth is driven predominantly by changes in HFC-125 emissions, which increase by 60.9%. In addition, HFC-32, although having the lowest GWP among the investigated HFCs, more than doubles between the two analysis windows (+116.6%), representing the strongest relative increase among the species considered. By comparison, HFC-134a changes only slightly (+1.8%), and HFC-143a remains essentially stable (−0.2%) over the period. The strong increase in HFC-32 is broadly consistent with the ongoing transition toward lower-GWP refrigerants in the refrigeration and air-conditioning sector. Similar to the trends observed in China, this increase likely reflects the gradual replacement of high-GWP refrigerant blends such as R-410A by more HFC-32–rich applications following the implementation of Kigali Amendment phasedown measures. The simultaneous growth in HFC-125 nevertheless suggests that blended refrigerants containing HFC-125 still remained widely used during the study period.

While both the prior and posterior indicate increasing U.S. HFC emissions over the study period, the prior suggests a substantially smaller rise in total emissions than inferred by the inversion. Total a priori emissions increase from 173.2 to 193.6 Tg $CO_2$ eq $yr^{-1}$, corresponding to a median gain of 20.4 Tg (+11.8%), compared to an increase of +42.0 Tg (+24.6%) in the posterior estimates. This difference is mainly driven by contrasting species-level trends in higher-impact gases. In the prior, both HFC-134a and HFC-143a show declining emissions (−25.1% and −12.1%, respectively), while the posterior reverses this tendency for HFC-134a and largely eliminates it for HFC-143a (−0.2%). HFC-23, the species with the highest GWP, shows a notably larger increase in the posterior than in the prior (+24.8% versus +7.4%). Considering posterior–prior differences averaged over 2015–2021, the United States shows a mixed pattern across species. Mean relative differences are modest and positive for HFC-32 (+3.1%), HFC-134a (+14.9%), and HFC-125 (+4.1%), while HFC-143a (−4.2%) and HFC-23 (−6.4%) exhibit slight negative adjustments, indicating generally small but species-dependent corrections relative to the prior. The statistics presented above, along with further details, are compiled in Table 2.

This project has received funding from the European Union's Horizon Europe research and innovation programme under grant agreement No 101081395

*Table 2. The same as Table 1 but for the United States.*

| Species / Metric | Posterior (kt $yr^{-1}$) 2015-2016 | Posterior (kt $yr^{-1}$) 2020-2021 | Posterior Relative Change | Prior (kt $yr^{-1}$) 2015-2016 | Prior (kt $yr^{-1}$) 2020-2021 | Prior Relative Change | Posterior vs Prior (Mean Relative Difference) |
|---|---|---|---|---|---|---|---|
| **HFC-125** | 14.3 (10.5–17.2) | 23.0 (20.2–24.8) | 60.9% | 12.9 | 22.4 | 73.1% | 4.1% |
| **HFC-134a** | 47.1 (39.4–54.0) | 47.9 (42.1–52.3) | 1.8% | 49.1 | 36.8 | -25.1% | 14.9% |
| **HFC-143a** | 5.8 (5.1–6.5) | 5.8 (5.3–6.6) | -0.2% | 6.5 | 5.7 | -12.1% | -4.2% |
| **HFC-32** | 7.7 (5.9–9.9) | 16.7 (13.4–18.5) | 116.6% | 7.2 | 17.6 | 143.1% | 3.1% |
| **HFC-23** | 0.4 (0.2–0.8) | 0.5 (0.2–0.8) | 24.9% | 0.46 | 0.49 | 7.4% | -6.4% |
| **Total $CO_2$-eq Emissions (Tg $CO_2$-eq $yr^{-1}$)** | 170.7 (136.4–203.8) | 212.8 (184.3–236.3) | 24.6% | 173.2 | 193.6 | 11.8% | — |

Except for HFC-23, the NID generally shows estimates comparable to the a priori emissions used in this study and, therefore, the above comparison largely also applies to the differences between our posterior estimates and NID values (Fig. 12). Similar to China, the localized nature of HFC-23 emissions likely induces a strong sensitivity of the inversion to the spatial distribution of a priori emissions, which in turn explains the considerable differences in posterior estimates (Fig. S6). However, in contrast to China, the EDGAR-based posterior HFC-23 estimates for the U.S. are systematically higher than those obtained using the GAINS inventory. Except for some trivial differences, similar to the results for China, the application of global constraints has little to no effect on the Posterior-GC estimates for the United States, which generally remain close to the unconstrained posterior estimates (Fig. 12). Due to the limited number of U.S.-specific top-down studies, a comprehensive comparison of our HFC estimates with the existing literature remains difficult. The only directly comparable estimate during our study period is the single-year 2014 estimate reported by Hu et al. (2017). Their results are broadly consistent with our posterior estimates for HFC-32 and HFC-125. Similar to the patterns found in our inversion, Hu et al. (2017) also suggest that prior inventories likely overestimate emissions of HFC-134a and HFC-143a. However, their posterior estimates for these two species are somewhat higher than those obtained in this study, although still within the corresponding uncertainty ranges, with reported values of 42.81 kt $yr^{-1}$ for HFC-134a (approximately +4 kt $yr^{-1}$, +10%) and 5.34 kt $yr^{-1}$ for HFC-143a (approximately +0.8 kt $yr^{-1}$, +22%).

For the US $SF_6$ emissions, inversion results (Fig.13) show a clearly declining emission trend of −0.054 kt $yr^{-1}$, dropping from 1.25 (1.06–1.58) kt in 2005 to 0.48 (0.36–0.71) kt in 2021. The decreasing trend is especially pronounced between 2008 and 2014, which coincides with the 2009 introduction of mandatory greenhouse gas reporting under the EPA's Greenhouse Gas Reporting Program for large $SF_6$

This project has received funding from the European Union's Horizon Europe research and innovation programme under grant agreement No 101081395

users (Ottinger et al., 2015). Our results are a bit higher compared to the regional inversion study by Hu et al. (2023); however, they show a remarkably similar declining trend in US $SF_6$ emissions between 2007 and 2018. Overall, a posteriori emissions are larger (by a factor of 2 on average) than the emissions reported to UNFCCC, but show better agreement in recent years (see Vojta et al. 2024).

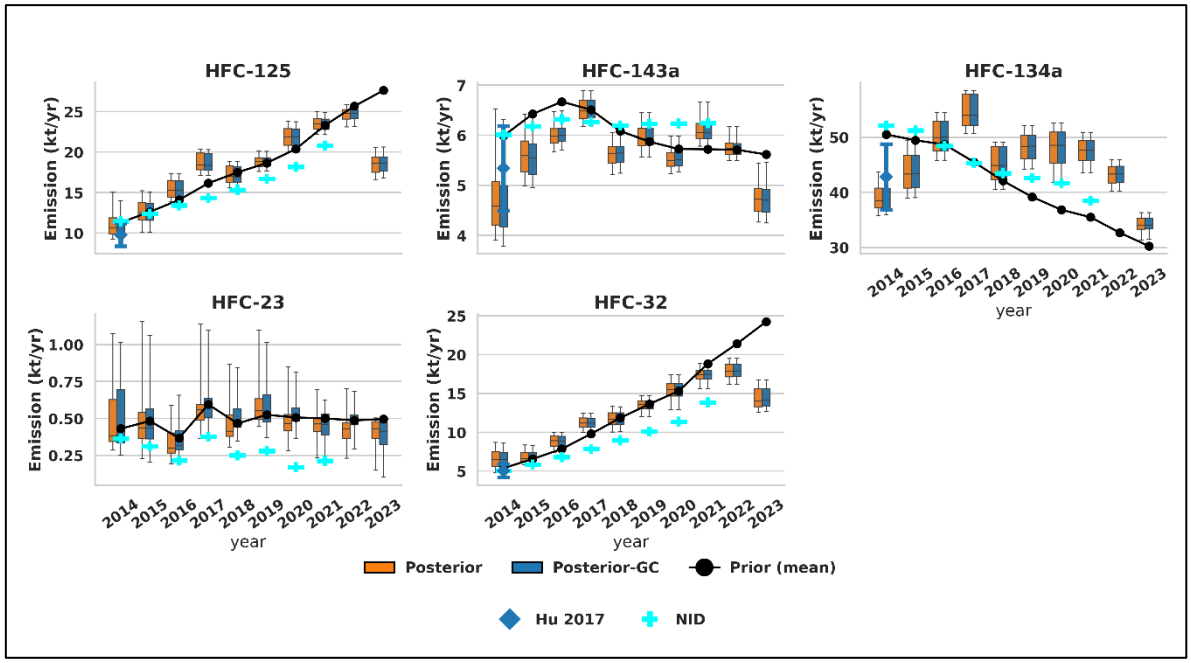


*Figure 12. US annual emissions (kt yr⁻¹) of five HFC species for 2014–2023. Layout and symbol definitions follow Fig. 10, while the literature estimates shown are specific to the US.*

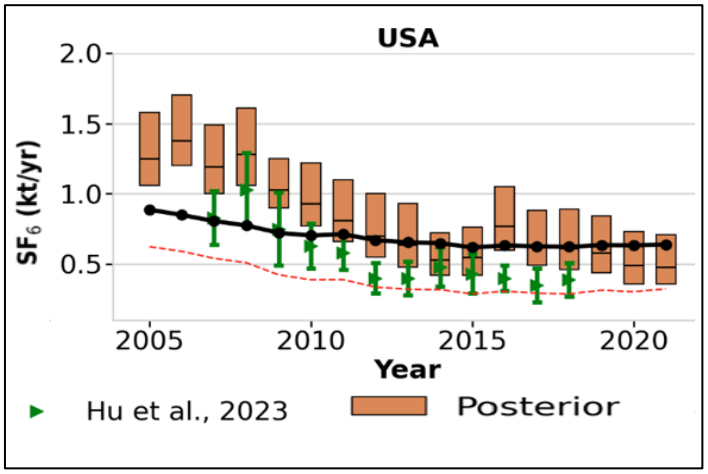


*Figure 13. Annual a posteriori $SF_6$ emission estimates for USA over 2005–2021. Coloured triangles represent estimated values from Hu et al. (2023, green). Black and Red lines represent reported a priori emissions and NID estimates reported values to UNFCCC, respectively.*

## Europe

For Europe, the inversion was conducted at two scales: as part of the 1° global inversion, and specifically at 0.5° in a regional inversion (shown by the orange and navy boxes for the former, and the black hatched boxes for the latter in Fig. 14). Overall, good consistency is found between the global and regional inversions. However, the higher-resolution regional inversions generally yield lower posterior emissions. This behaviour is likely related to the increased flexibility of the inversion to fit the

This project has received funding from the European Union's Horizon Europe research and innovation programme under grant agreement No 101081395

measurements within a finer emission space in the regional setup. At finer spatial resolution, each grid cell represents a smaller area, allowing emission corrections to be applied with higher spatial discrimination. It can also be partly attributed to the stronger influence of the optimized baseline field in the regional setup. As spatial resolution increases, the number of emission parameters grows substantially while the observational information content remains relatively similar, leading to weaker constraints on individual grid cells and stronger correlations among neighbouring emission parameters. Under these conditions, part of the model–observation mismatch can be more efficiently accommodated through adjustments of the optimized baseline field, which affects many observations coherently over large spatial scales. Consequently, a larger fraction of the mismatch may be attributed to baseline adjustments (upward in this case) rather than regional emission increments, contributing to systematically higher optimized baseline fields and reduced adjustments in emission variables. Although no straightforward metric exists to determine which inversion more closely reflects the true emissions, we report the HFC estimates from the regional inversion for brevity. This choice is motivated primarily by the improved spatial resolution of emission patterns in the regional framework, which allows for a more detailed and physically interpretable representation of spatial heterogeneity. In addition, the regional inversion tends to produce smoother and more physically plausible year-to-year variability compared to the global inversion. The global setup, due to its coarser aggregation and stronger sensitivity to large-scale compensating errors, exhibits more pronounced interannual fluctuations that are more likely to reflect artefacts of limited spatial degrees of freedom rather than genuine emission changes. In contrast, the regional inversion distributes the observational constraints over a larger number of parameters, which reduces the tendency for abrupt temporal swings and yields a more stable temporal evolution that is consistent with expected emission behaviour.

Across 2015–2016 to 2020–2021, the European inversion yields consistently higher absolute $CO_2$-eq HFC emissions than the prior, although both datasets show a clear declining trend. In the regional inversion, total emissions decrease from 145.9 to 126.0 Tg $CO_2$-eq $yr^{-1}$, corresponding to a reduction of 20.0 Tg (13.7%), whereas the prior decreases from 99.6 to 81.5 Tg $CO_2$-eq $yr^{-1}$ (18.2%). At the species level, the results indicate a transition characterized by moderate growth in HFC-32 alongside continued declines in major legacy HFCs. HFC-32 increases from 4.96 to 7.7 Tg in the regional inversion (+55%), consistent with the ongoing transition toward lower-GWP refrigerants, although the increase remains smaller than suggested by the prior. HFC-134a and HFC-143a decrease by 13% and 37%, respectively, while HFC-125 remains nearly unchanged over the study period. HFC-23 exhibits little temporal variability and remains almost stable throughout the analysis period. Overall, the results indicate a transition in the European refrigerant sector characterized by increasing HFC-32 use alongside declining emissions of legacy gases.

Regarding differences in average emission levels, the regional posterior estimates remain approximately 51% higher than the prior in terms of total $CO_2$-eq HFC emissions. This systematic enhancement is reflected across individual species, with mean posterior increases relative to the prior of about 61% for HFC-143a, 48% for HFC-125, 43% for HFC-134a, and around 29% for both HFC-32 and HFC-23. Regarding the global total constraint, as expected for the relatively well-monitored European domain, it has only a minor influence on the posterior estimates.

Unlike the results for the United States and China, the European estimates show a noticeable sensitivity to the choice of prior inventory across all HFC species (Fig. S6). For instance, using GAINS as prior information generally leads to lower posterior estimates, particularly for HFC-32, for which emissions decrease by about 20–30%. This sensitivity reflects differences in the underlying prior assumptions, as GAINS reports lower baseline emissions for most HFC species in Europe and also differs in the spatial distribution of major emission hotspots (Fig. 5). Nevertheless, even when GAINS is used as prior information, the resulting posterior estimates remain substantially higher than the corresponding prior values, NID estimates, and the estimates reported in the recent preprint study by De Longueville et al.

This project has received funding from the European Union's Horizon Europe research and innovation programme under grant agreement No 101081395

(2026). This discrepancy is likely related to differences in baseline treatment. Unlike our approach, the latter study derives baseline mole fractions using REBS and a site-specific method following Manning et al. (2021), which accounts for time-varying background concentrations and air mass origins. In a comparison study, Vojta et al. (2022) already showed that REBS tends to overestimate the baseline, and that this effect increases with longer back-trajectory horizons, which in turn leads to underestimated emissions.

To clarify whether the lower emissions reported by De Longueville et al. (2026) may be due to their different baseline treatment, we performed a sensitivity experiment for the regional inversion using a REBS-derived baseline for HFC-134a over the period 2017–2019. Since the study by De Longueville et al. (2026 preprint) and its associated outputs became available only very recently, we instead used the REBS estimates from Annadate et al. (2025) for further investigation. They also used REBS for baseline estimation but only for HFC-134a, with a 10-day back-trajectory (instead of 30 days in De Longueville et al. (2026) and reported emission estimates for a domain of 22 major European emitting countries, which are also clearly lower than ours. Figure 15-A shows sensitivity inversions using a REBS-based baseline at the regional scale, using the same inversion setup as our regional HFC-134a inversion, except for the use of 10-day backward trajectories for SRR. Notably, we are able to reproduce the emission estimates reported by Annadate et al. (2025) using the REBS-derived baseline. This is despite differences between the latter study and our study in prior assumptions (EDGARv8 versus GAINS- and EDGAR-scaled priors) and prior uncertainties (100% versus 200%). To assess which approach better represents the true baseline, Fig. 15-B compares the mean bias error (MBE) between observed and prior mixing ratios derived using the REBS and FP-LCM baselines. The REBS-derived prior shows a systematic positive bias across all sites, most pronounced at TAC, consistent with previous findings that REBS-based inversions tend to yield higher baseline contributions and thus lower emission estimates. In contrast, the FP-LCM prior exhibits a more balanced spatial distribution of biases across stations, although systematic errors cannot be ruled out. A negative bias is likely, particularly at TAC and CMN, driven not only by baseline underestimation but also by transport errors, such as misrepresentation of boundary layer height and unresolved local plumes, in our relatively coarse-resolution framework. It is worth noting that the REBS baseline exhibits a stronger posterior correction (i.e. lower posterior-to-prior consistency) at the background station MHD (Fig. S7, top panel) compared with FP-LCM (Fig. S7, middle panel). As shown in Fig. 15-A, the estimates from De Longueville et al. (2026) are lower than those of Annadate et al. (2025), likely reflecting the fact that the REBS baseline cannot be chosen independently of the backward simulation period. This can lead to increased prior concentrations in a 30-day backward trajectory (compared to the 10-day window used in Annadate et al. (2025)) and, consequently, to an underestimation of posterior estimates.

Disentangling the extent to which the inversion corrects potential biases in each baseline toward a more realistic state, or instead compensates for remaining model–observation mismatches, is not straightforward. Nevertheless, several pieces of evidence provide a consistent picture. Previous studies and our sensitivity analysis suggest that REBS tends to overestimate baseline contributions, and our results for the United States and China agree well with earlier work. Taken together, the inversion using the FP-LCM baseline seems to yield a more robust separation of baseline and local signals compared with the REBS-based setup. This interpretation is further supported by the fact that the FP-LCM baseline using 50-day backward trajectories for the global and regional inversions performs better than the 10-day setup used in the sensitivity inversions (unlike data-driven baselines such as REBS). As shown in Fig. S8, the 50-day backward trajectory configuration reduces the mean bias error (MBE) between observations and prior mixing ratios, while also leading to closer agreement between the FP-LCM prior and posterior baselines (Fig. S7, bottom panel). This improvement mainly reflects the reduced influence of the coarse-resolution baseline and outside-domain signals (the latter driven by coarse outside-domain emission estimates) on the total concentration and, in turn, the increased contribution of high-resolution

This project has received funding from the European Union's Horizon Europe research and innovation programme under grant agreement No 101081395

inside-domain signals, leading to better separation between background and local emissions in the 50-day backward trajectory configuration compared to the 10-day configuration.

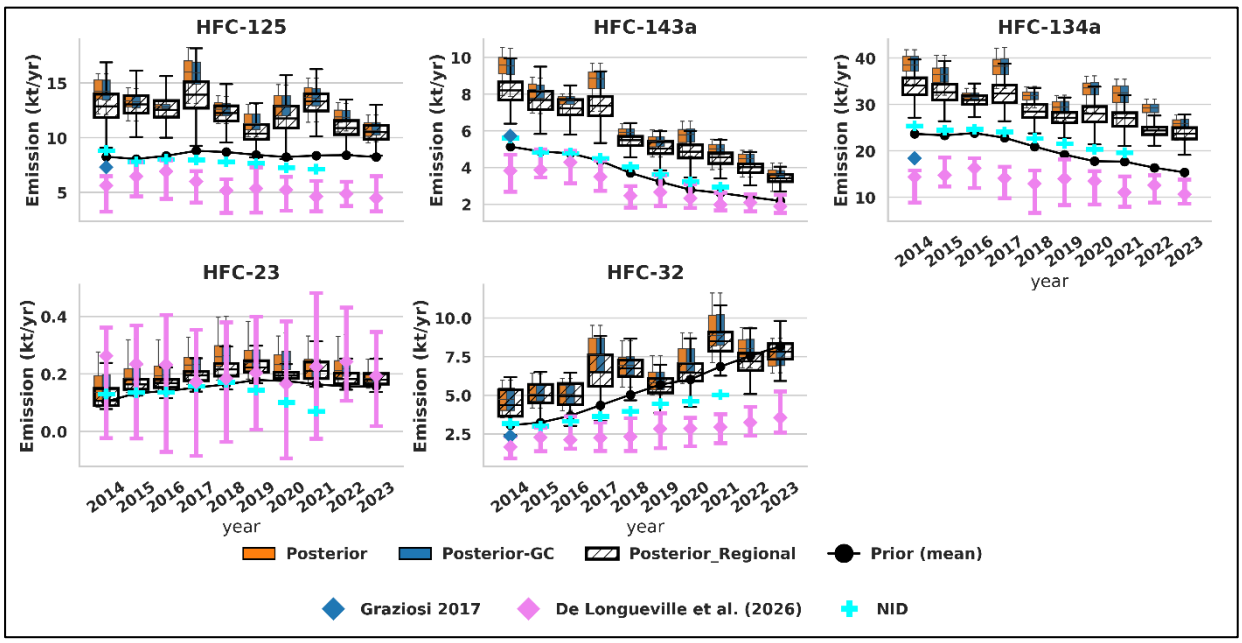


*Figure 14. Annual emissions (kt yr⁻¹) of five HFC species in Europe for 2014–2023. Symbol definitions are the same as in Fig. 10. Black hatched boxes denote regional inversion estimates, while the posterior (orange) and posterior-GC (navy) results are derived from global-scale inversions.*

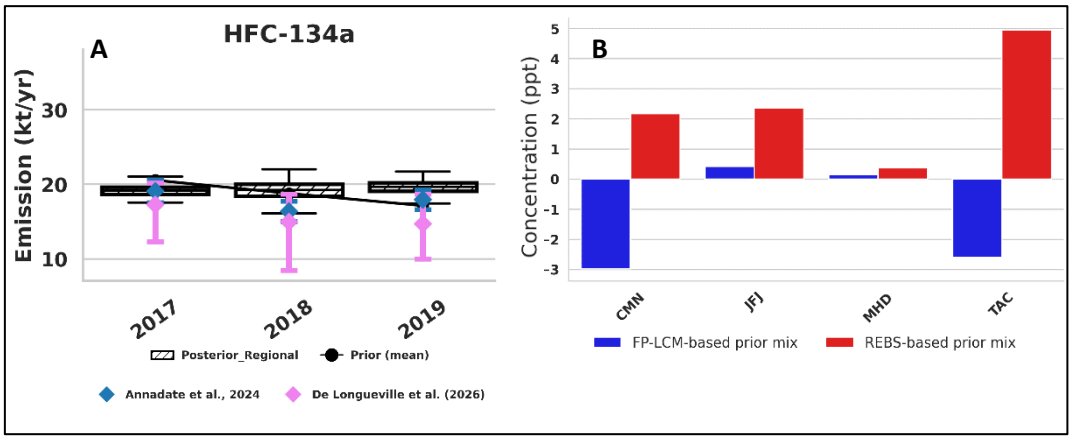


*Figure 15. (A) Regional-scale inversion of HFC-134a (black hatched boxes) in Europe-22 (as defined by Annadate et al. (2025)) using a REBS-based baseline computed with a 10-day back trajectory. Note that in (A), only regional emissions based on REBS are shown; regional FP-LCM-based emission estimates are not shown for clarity. (B) shows the mean bias error (MBE) between the observed mixing ratios and the prior mixing ratios calculated with FP-LCM (blue) and REBS (red), respectively, both using a 10-day backward trajectory.*

For $SF_6$, the annual aggregated emissions from EU-27 countries (Fig. 16) show a decreasing trend of −0.006 kt $yr^{-1}$, dropping from 0.41 (0.35–0.46) kt in 2005 to 0.25 (0.22–0.29) kt in 2021. While a posteriori emissions are relatively stable and exceed the a priori emissions until 2017, there is a significant drop in 2018, after which they are closer to the a priori emissions. It seems plausible that this drop in $SF_6$ emissions in 2018 was a result of the EU's F-gas regulation 517/2014, which required new electrical switch gear with a leak detection system to be put into service from 2017 onwards and banned the use of $SF_6$ for recycling magnesium die-casting alloys as of 2018. In Vojta et al. (2025), we further demonstrate that the 2017–2018 drop is also evident in emission trends over southern Germany, indicating the influence of regional regulatory actions. This major emission source, not represented in

This project has received funding from the European Union's Horizon Europe research and innovation programme under grant agreement No 101081395

the German reports, was further quantified in collaboration with the PARIS project (Meixner et al., 2025). The regional $SF_6$ inversion (Vojta et al. 2025) yields results that are very similar to those of the global inversion, particularly for the more recent years when observational coverage is improved. The emission drop between 2017 and 2018 is also reproduced and appears even more pronounced, which may be attributable to the higher spatial resolution. Before this drop, a posteriori emissions are larger than the emissions reported to UNFCCC, but show a good agreement in recent years (see also Vojta et al. 2024, 2025).

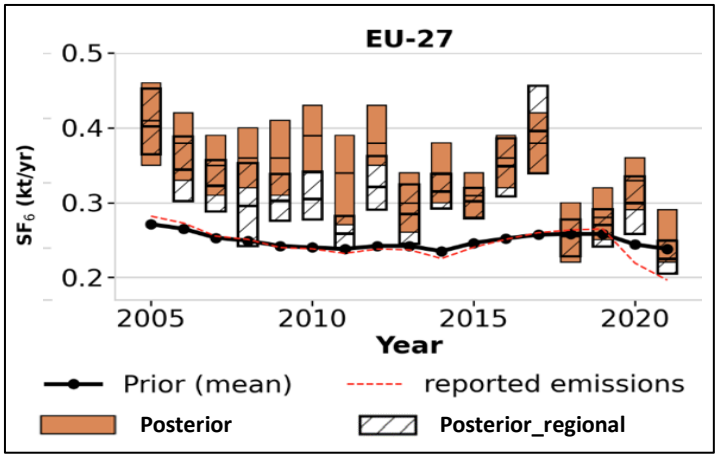


*Figure 16. Annual a posteriori $SF_6$ emission estimates (orange boxes) for EU-27 countries for the period 2005–2021. Hatched boxes indicate results from the high-resolution European regional-scale inversion. The red line represents emissions reported to the UNFCCC (NID).*

In the following, we discuss the emission trends of HFCs and $SF_6$ and their relative differences relative to the prior for the United Kingdom, Germany, and France, which represent some of the major contributors to total emissions within the European region. We then summarize the posterior estimates for these and other major European emitters in Tables 3 and 4. It is worth noting that the posterior estimates reported here are derived from the regional inversion.

**United Kingdom**

Over the period 2015–2016 to 2020–2021, the United Kingdom shows a clear and robust decline in total HFC $CO_2$-equivalent emissions when estimated using the regional inversion framework. Total emissions decrease from 21.1 Tg $CO_2$-eq $yr^{-1}$ (18.4–23.1) to 13.7 (12.3–15.4), corresponding to an approximate 35% reduction at the median. The prior also indicates a decline in total emissions, although at a lower absolute level and with a weaker reduction (14.3 to 11.6 Tg $CO_2$-eq $yr^{-1}$). At the species level, the dominant driver of the national trend is HFC-134a. The posterior shows a substantial median decrease from 5.6 to 3.7 kt $yr^{-1}$, while the prior also shows a weaker decline from a lower level. This decline is physically consistent with the continued phase-down of high-GWP refrigerants in mobile air conditioning and refrigeration systems, driven by both regulatory pressure and gradual turnover of existing equipment banks. HFC-32 shows a contrasting but smaller-scale upward trend, increasing from 0.4 to 0.7 kt $yr^{-1}$. The prior similarly indicates a strong increase, although slightly larger in magnitude (0.508 to 0.878 kt $yr^{-1}$). This agreement in direction reflects the ongoing transition toward lower-GWP refrigerants, consistent with patterns observed across all major global emitting regions. HFC-23 remains negligible in magnitude, with only minimal variation across the two windows (around 0.004 to 0.003 kt $yr^{-1}$). It is worth noting that the global constraint (Posterior-GC) has little influence on the UK estimates from the global inversion, which remain in close agreement with the regional inversion (Fig. 17). The systematic upward correction of HFC emissions observed across Europe over 2015–2021, except for

This project has received funding from the European Union's Horizon Europe research and innovation programme under grant agreement No 101081395

HFC-32, is also evident in the UK, as reflected in the relative differences: positive values for HFC-134a (+42.8%), HFC-143a (+35.2%), and HFC-125 (+21.0%), and a negative value for HFC-32 (−15.2%). No robust relative difference is found for HFC-23 due to its very low magnitude. UK estimates are also systematically higher than those reported in the literature by Manning et al. (2021) and De Longueville et al. (2026), likely reflecting differences in baseline treatment as discussed above. Nevertheless, despite differences in absolute magnitude and the direction of posterior adjustments, two robust features are consistently observed across both this study and the literature. First, a pronounced peak in emissions of HFC-125, HFC-134a, and HFC-143a occurs at the beginning of the study period, with the maximum generally around 2015 (also reported by Annadate et al. (2025)), although exact timing may vary by ±1 year. This pattern is likely linked to market dynamics under the EU F-gas and MAC regulations, where firms may have front-loaded HFC purchases ahead of progressively tightening quota constraints. Second, a decline in emissions is observed around 2019–2020 across all major HFC species, bringing estimates closer to NID values. While this feature is consistent with the ongoing impact of the EU F-gas phase-down, a minor additional contribution from COVID-19-related disruptions cannot be excluded, particularly due to reduced servicing and installation activity during 2020. UK total greenhouse gas emissions also decreased substantially in 2020 (on the order of ~8–9%), largely driven by reduced transport and industrial activity (BEIS, 2022).

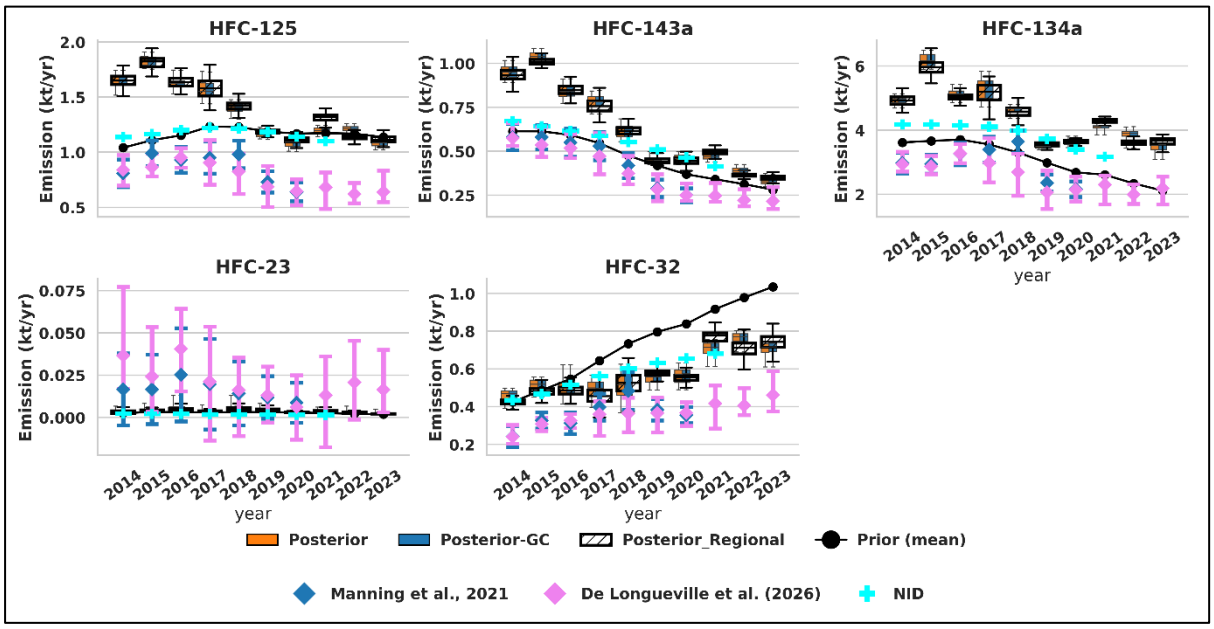


*Figure 17. Same as Figure 10, but for HFC emission estimates in the United Kingdom.*

For $SF_6$, UK emissions (Fig. 18) declined from 38 (31–46) t $yr^{-1}$ in 2005 to 19 (15–26) t $yr^{-1}$ by 2021, with a substantial drop from 68 (47–77) t $yr^{-1}$ in 2008 to 19 (15–26) t $yr^{-1}$ in 2018, corresponding to an average annual decrease of −3.2 t $yr^{-1}$. The substantial decrease in emissions observed after 2008 is likely a result of the 2006 EU F-gas regulations, with most bans coming into effect in 2008. Although inversion results exceed the reported values between 2005 and 2017, they align closely from 2018 onward. While our results are slightly higher than the estimates of Ganesan et al. (2014) in 2012, and Brunner et al. (2017) in 2011, they are in excellent agreement with the results of Manning et al. (2022) for the whole study period, particularly from 2012 onward, when uncertainties also become significantly smaller due to a better observational coverage. This good agreement is a particularly noteworthy result, as the inversion system used by Manning et al. (2022) differs significantly from ours. Their approach employs the InTEM inversion technique (Manning et al. (2011) and Manning et al. (2021)), with a priori

This project has received funding from the European Union's Horizon Europe research and innovation programme under grant agreement No 101081395

emissions uniformly distributed across the country, large a priori emission uncertainties, and inversion intervals of 1 and 3 months.

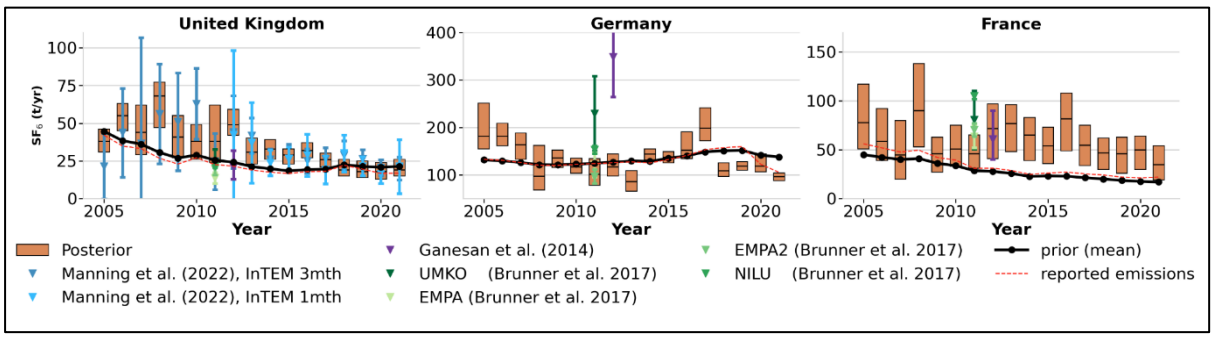


*Figure 18: Annual posterior SF6 emission time series for the United Kingdom, Germany, and France (orange boxes), with their respective uncertainties defined as 2.5/97.5th percentiles. Coloured triangles represent estimated values from previous inverse model studies, black dots represent the prior averaged over different inventories, while the red dashed line represents reported values to UNFCCC (NID).*

### Germany

Germany displays a fundamentally different emission evolution compared to the UK, characterized by a slight but consistent increase in total HFC $CO_2$-eq emissions between 2015–2016 and 2020–2021. Total emissions rise from 15.6 to 16.5 Tg $CO_2$-eq $yr^{-1}$, indicating a modest upward trend rather than a decline. This behaviour contrasts sharply with the prior, which suggests a strong decrease from 11.8 to 8.9 Tg $CO_2$-eq $yr^{-1}$. The inversion, therefore, not only increases absolute emission levels but also reverses the direction of the temporal trend. As with other major emitting regions, HFC-32 emissions are found to be upward corrected and increasing over the study period. The posterior increases from 0.2 to 0.7 kt $yr^{-1}$, consistent with the prior, which also increases but to a smaller extent (from 0.2 to 0.5 kt $yr^{-1}$). This suggests that Germany is undergoing a stronger-than-expected transition toward HFC-32-based systems, likely associated with rapid deployment of heat pumps (Glaesmann, 2023). While HFC-125 also increases, from 0.96 to 1.5 kt $yr^{-1}$, HFC-134a and HFC-143a behave differently, showing a mild decline in the regional inversion (from 5.1 to 4.7 kt $yr^{-1}$ and from 0.7 to 0.6 kt $yr^{-1}$, respectively), although remaining substantially above prior estimates. This indicates that while the transition away from HFC-134a and HFC-143a is underway, its absolute emissions remain underestimated in inventories. HFC-23 remains small and relatively stable, with only minor fluctuations that do not materially influence total emissions. The global constraint again plays a negligible role in the inversion results (Fig. 19). Overall, Germany exhibits a transition-dominated but still growing HFC system, where rapid uptake of HFC-32 coexists with persistent emissions from legacy blended refrigerants. De Longueville et al. (2026 preprint) report emissions that are generally lower and closer to the prior and NID, compared with the posterior estimates from our inversion. Available estimates specifically for HFC-23 from Simmonds et al. (2018) and UNEP (2024) indicate very low emission levels, broadly consistent with our results. However, UNEP (2024) is deviating from our estimates reporting near-zero estimates from 2019 onward.

This project has received funding from the European Union's Horizon Europe research and innovation programme under grant agreement No 101081395

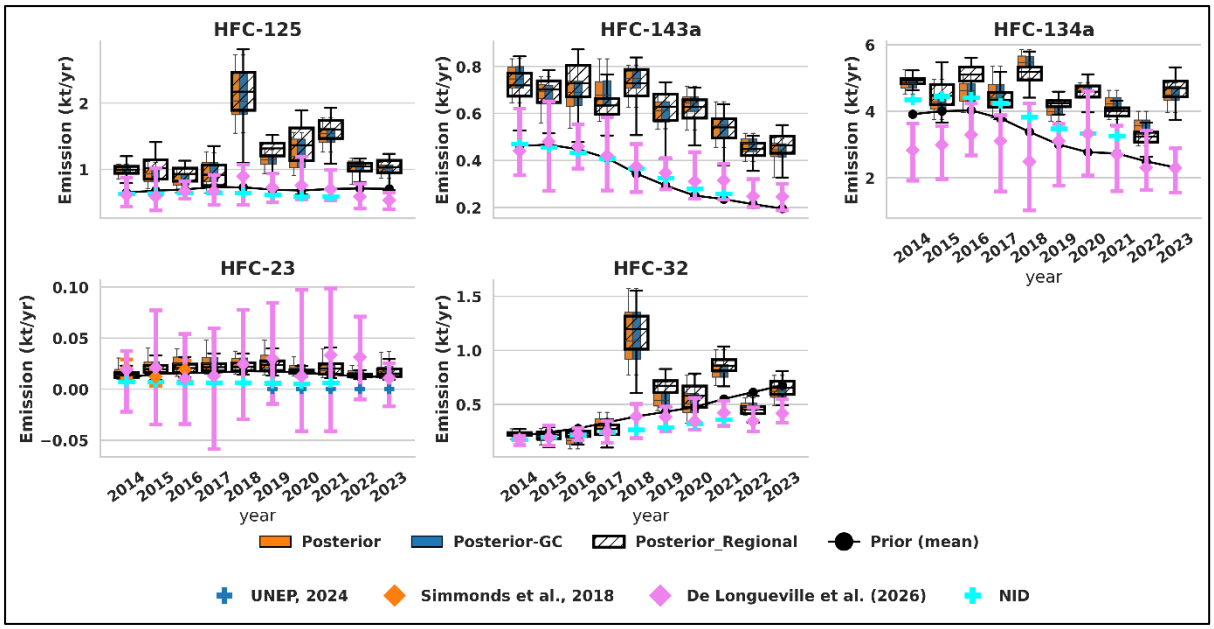


*Figure 19. As in Figure 10, but showing HFC emission estimates for Germany.*

For $SF_6$, German emissions (Fig. 20) show a decline in emissions from 182 (155–251) t $yr^{-1}$ in 2005 to 86 (66–109) t $yr^{-1}$ in 2013. Afterwards, emissions increased significantly, peaking at 199 (172–241) in 2017. This was followed by a sharp drop to 109 (97–125) t $yr^{-1}$ in 2018, after which emissions stabilized. Over the entire study period, emissions decreased from 182 (155–251) t $yr^{-1}$ in 2005 to 97 (88–104) t $yr^{-1}$ in 2021. Overall, the German a posteriori emissions align well with the values reported to the UNFCCC, however, the inversion results reveal distinct emission trends during specific time periods that are not reflected in the reported data. Our results for Germany agree well with three of the four inversions performed in Brunner et al. (2017), but give much lower emissions than those estimated by Ganesan et al. (2014). However, their high estimates were likely a result of the use of excessive German a priori emissions (~ 650 t $yr^{-1}$), which were based on the EDGAR v4.2 inventory. Although their German a posteriori emissions were substantially lower than their a priori values, the inversion likely could not fully correct the huge bias present in this version of the EDGAR inventory. Note, that Germany is the largest $SF_6$ emitter in Europe and therefore strongly shaping the European emission trend.

### France

For France, total HFC emissions declined from about 30 to 27 Tg $CO_2$-eq $yr^{-1}$, indicating a moderate reduction over the period. The prior suggests a stronger decrease (20.7 to 13.8 Tg $CO_2$-eq $yr^{-1}$). France reflects a clear transition in refrigerant use. HFC-32 increases from about 1.1 to 1.9 kt $yr^{-1}$, and HFC-125 rises from about 2.5 to 2.9 kt $yr^{-1}$, consistent with growing adoption of low-GWP alternatives and continued emissions from blended refrigerant banks. In contrast, HFC-134a declines from about 6.7 to 5.1 kt $yr^{-1}$ and HFC-143a from about 1.5 to 1.1 kt $yr^{-1}$, reflecting the ongoing phase-down of legacy refrigerants. HFC-23 decreases but remains negligible in the national total. Overall, France exhibits a mixed transition system where reductions in high-GWP species are partly offset by increases in replacement gases, resulting in a moderate net decline in total emissions but systematically higher inversion-based levels than the prior. Except for the relative consistency with near-zero HFC-23 estimates reported by Simmonds et al. (2018) and UNEP (2024), our estimates for France are clearly higher than those from the NID and De Longueville et al. (2026 preprint) across the study period.

This project has received funding from the European Union's Horizon Europe research and innovation programme under grant agreement No 101081395

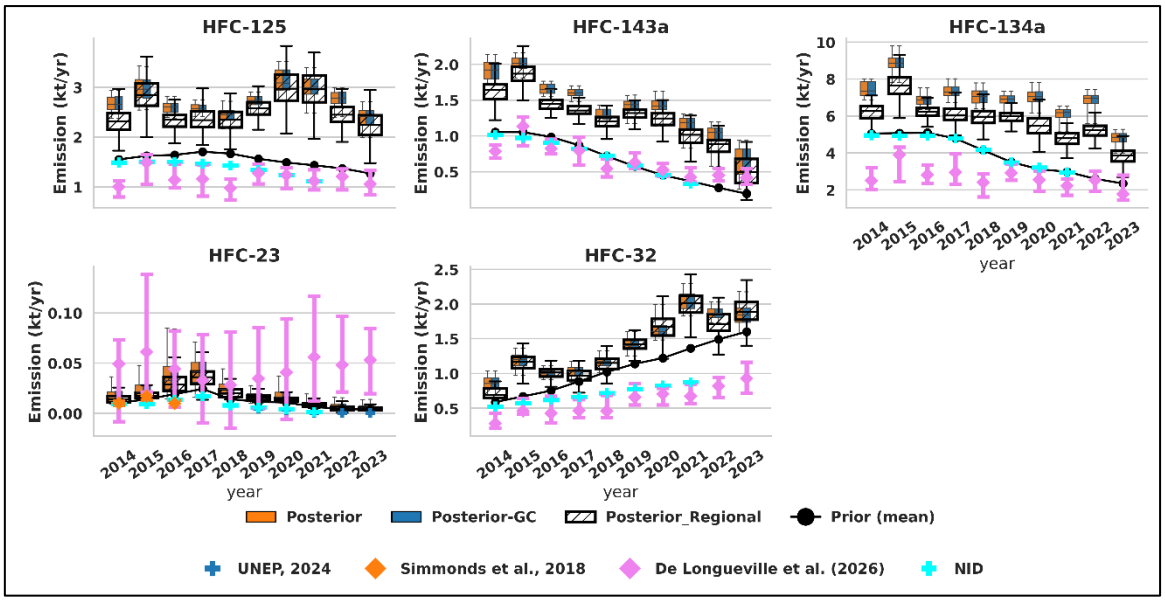


*Figure 20. As in Figure 10, but showing HFC emission estimates for France.*

$SF_6$ emissions in France (Fig. 21), declined from 78 (51–117) t $yr^{-1}$ in 2005 to 35 (19–54) t $yr^{-1}$ in 2021, with an average annual decrease of −1.2 t $yr^{-1}$. Our results exceed the reported values throughout the whole study period while they are in good agreement with Ganesan et al. (2014), and the lower estimates of Brunner et al. (2017).

We further report snapshot posterior emissions with low–high ranges (kt $yr^{-1}$) for 2016 and 2023 ($SF_6$ to 2021) in the following tables. Estimates for Europe, North-West (NW) Europe, GBR, FRA, DEU, and EU-27 are derived from the regional inversion, whereas those for the USA and China are derived from the global inversion. Broadly, Europe shows declines in HFC-134a, HFC-143a, and HFC-125, with a slight increase in HFC-32. In the USA, HFC-32 and HFC-125 increase, whereas HFC-143a shows a modest decline. China exhibits increases across all HFC species. $SF_6$ displays clear regional contrasts: Europe decreases (EU-27: 0.35 to 0.23 kt $yr^{-1}$; NW Europe: 0.28 to 0.16; DEU: 0.15 to 0.097; GBR: 0.026 to 0.019; FRA: 0.082 to 0.035), while China increases (3.58 to 5.16) and the USA declines (0.77 to 0.48). For further detail, refer to Table 3 for HFC-134a, HFC-143a, and HFC-125, and Table 4 for HFC-32, HFC-23, and $SF_6$, which report region-specific emissions and percent changes.

This project has received funding from the European Union's Horizon Europe research and innovation programme under grant agreement No 101081395

*Table 3: Entries are median (low–high); the middle value is the median. Units: kt/yr. Europe (NW Europe, GBR, FRA, DEU, EU-27) uses the regional inversion; USA and China use the global inversion. Δ [%]: median percent change (HFCs 2016 → 2023; SF6 2016 → 2021). Uncertainty conventions differ for HFCs versus $SF_6$, see main text for quantile definitions and interval interpretation*

| Region | HFC-32 | | | HFC-23 | | | SF6 | | |
|---|---|---|---|---|---|---|---|---|---|
| | 2016 | 2023 | Δ [%] | 2016 | 2023 | Δ [%] | 2016 | 2021 | Δ [%] |
| NW Europe | 1.6 (1.4–1.7) | 3.1 (2.7–3.5) | 97.1 | 0.076 (0.047–0.127) | 0.053 (0.036–0.071) | -30.6 | 0.28 (0.24–0.34) | 0.16 (0.15–0.19) | -43 |
| GBR | 0.5 (0.4–0.5) | 0.7 (0.6–0.8) | 53.1 | 0.004 (0.003–0.008) | 0.003 (0.002–0.003) | -25 | 0.026 (0.021–0.030) | 0.019 (0.015–0.026) | -27 |
| FRA | 1.0 (0.9–1.2) | 1.9 (1.6–2.3) | 85.7 | 0.029 (0.013–0.048) | 0.011 (0.004–0.019) | -62.1 | 0.082 (0.049–0.108) | 0.035 (0.019–0.054) | -57 |
| DEU | 0.2 (0.2–0.3) | 0.7 (0.5–0.8) | 182.8 | 0.021 (0.012–0.029) | 0.015 (0.010–0.028) | -28.6 | 0.15 (0.13–0.19) | 0.097 (0.088–0.104) | -36 |
| Europe (EU-27) | 4.4 (3.7–5.1) | 7.2 (6.3–8.5) | 64.7 | 0.154 (0.118–0.199) | 0.140 (0.106–0.209) | -9.1 | 0.35 (0.29–0.44) | 0.23 (0.19–0.26) | -36 |
| USA | 8.9 (7.4–10.0) | 14.0 (12.5–16.8) | 57.9 | 0.3 (0.2–0.6) | 0.4 (0.1–0.5) | 43.5 | 0.77 (0.60–1.05) | 0.48 (0.36–0.71) | -60 |
| China | 12.0 (9.9–15.4) | 32.2 (24.3–41.5) | 167.8 | 9.6 (4.9–13.2) | 14.6 (11.6–17.6) | 51.6 | 3.58 (3.26–3.90) | 5.16 (4.75–5.60) | +44 |

This project has received funding from the European Union's Horizon Europe research and innovation programme under grant agreement No 101081395

*Table 4: Same conventions as Table 1, but for HFC-32, HFC-23, and $SF_6$.*

| Region | HFC-134a | | | HFC-143a | | | HFC-125 | | |
|---|---|---|---|---|---|---|---|---|---|
| | 2016 | 2023 | Δ [%] | 2016 | 2023 | Δ [%] | 2016 | 2023 | Δ [%] |
| NW Europe | 14.4 (13.3–15.2) | 10.7 (9.1–11.9) | -26 | 2.9 (2.7–3.1) | 1.3 (0.8–1.6) | -55.3 | 4.4 (3.9–4.7) | 4.1 (3.4–4.8) | -6.1 |
| GBR | 5.0 (4.9–5.2) | 3.7 (3.3–3.8) | -27 | 0.8 (0.8–0.9) | 0.3 (0.3–0.4) | -58.9 | 1.6 (1.6–1.7) | 1.1 (1.1–1.2) | -32 |
| FRA | 6.2 (5.7–6.7) | 3.9 (3.1–4.6) | -38 | 1.4 (1.3–1.6) | 0.5 (0.2–0.8) | -65.6 | 2.3 (2.1–2.6) | 2.2 (1.7–2.8) | -4.5 |
| DEU | 5.1 (4.7–5.5) | 4.7 (3.9–5.1) | -8 | 0.7 (0.6–0.9) | 0.5 (0.3–0.5) | -36.3 | 0.9 (0.7–1.1) | 1.0 (0.9–1.2) | 11.2 |
| Europe (EU-27) | 29.3 (27.0–31.6) | 21.9 (18.7–24.6) | -25 | 6.8 (6.0–7.3) | 3.2 (2.4–3.5) | -53.3 | 11.5 (10.0–12.8) | 9.6 (8.2–11.4) | -16.2 |
| USA | 50.0 (45.8–54.6) | 34.0 (31.4–36.3) | -32 | 6.0 (5.7–6.5) | 4.7 (4.3–5.5) | -21 | 15.3 (13.9–17.4) | 18.6 (16.6–20.6) | 21.6 |
| China | 29.4 (24.8–33.4) | 41.9 (30.0–48.2) | 42.6 | 3.2 (2.3–3.7) | 6.2 (4.1–8.9) | 94.9 | 11.6 (8.5–14.1) | 22.3 (15.0–27.1) | 93.1 |

# 4. Conclusions

- **Chinese F-gas emissions**

  China remains the largest global emitter of HFCs in terms of $CO_2$-equivalent emissions, and our inversion results indicate a continued upward trend during the study period. Total posterior HFC emissions increase from 273.0 (166.1–362.2) to 323.8 (231.6–397.9) Tg $CO_2$-eq $yr^{-1}$ between 2015–2016 and 2020–2021, corresponding to an increase of about 19%. The strongest relative growth is found for HFC-32, which increases by nearly 90%, while HFC-143a is the only species showing a slight decline. China formally accepted the Kigali Amendment in 2021, committing to a phasedown of HFC production and consumption, with a production and consumption freeze scheduled for 2024 (Fang et al. (2026). Since our analysis period ends in 2023, future work will be important to evaluate how the emission trends identified here evolve under the implementation of these regulatory measures. Although the prior inventories indicate a similar overall direction of change, they systematically suggest substantially stronger growth than inferred by the inversion, particularly for HFC-32, HFC-125, and HFC-134a. Additionally, posterior emissions remain consistently lower than the prior across all investigated HFC species. The observed increase in HFC-32 is consistent with the ongoing transition toward lower-GWP refrigerants under the Kigali Amendment, particularly through the growing adoption of HFC-32-based cooling systems. As China represents one of the largest global producers and consumers of refrigeration and air-conditioning technologies, this transition likely plays a central role in shaping the observed emission trends. At the same time, the weaker posterior growth relative to the prior suggests that current inventories may overestimate the pace of emission increases associated with this transition. Our posterior estimates generally agree well with recent top-down studies by Fang et al. (2026), despite methodological differences in baseline treatment and

This project has received funding from the European Union's Horizon Europe research and innovation programme under grant agreement No 101081395

prior uncertainties. For HFC-23, however, our estimates remain substantially higher than the near-zero bottom-up estimates reported by UNEP (2024), while remaining more consistent with independent top-down estimates from eastern China reported by Park et al. (2023). China is also the largest emitter of $SF_6$, accounting for roughly half of the global total emissions. Consequently, various studies - both, bottom-up and top-down - have been investigating the Chinese emission trend in recent years (e.g. An et al. (2024); Fang et al. (2014); Guo et al. (2023); Simmonds et al. (2020)). All of these studies found a substantial increase in Chinese emissions in the 21th century, however the determined magnitudes cover a wide range. We confirmed the upward Chinese emission trend and provided emission estimates updated to the year 2021 showing remarkable agreement with the latest regional inversion study by An et al. (2024). This agreement is noteworthy, as An et al. (2024) did not only employ a different inversion system, but also used a different observation network from inside China. The similarity of results, despite the different inversion set-up, is reassuring and underscores the reliability of these estimates. Another finding is that the growth of Chinese $SF_6$ emissions has slightly slowed down since the mid-2010s, suggesting that Chinese regulations implemented 2012 and 2015 had a positive effect. However, achieving substantial reductions will require more stringent measures, such as those implemented in the EU or in the U.S. which could have substantial impact on the global total $SF_6$ emissions.

- **U.S. F-gas emissions**

  The United States shows a substantial increase in total HFC emissions over the study period, with posterior $CO_2$-equivalent emissions increasing from 170.7 (136.4–203.8) to 212.8 (184.3–236.3) Tg $CO_2$-eq $yr^{-1}$ between 2015–2016 and 2020–2021. This increase is driven primarily by HFC-125 and HFC-32, with the latter more than doubling over the analysis period. The pronounced increase in HFC-32 is consistent with the ongoing replacement of higher-GWP refrigerants such as R-410A by HFC-32-rich systems following Kigali Amendment implementation and broader refrigerant transitions within the cooling sector. At the same time, continued growth in HFC-125 indicates that blended refrigerants containing HFC-125 remained widely used during the study period. HFC-134a and HFC-143a remain relatively stable in the posterior estimates, whereas the prior suggests decreasing emissions for these two species. These results suggest that inventories may overestimate the rate of phase-down for some legacy refrigerants. Unlike China and Europe, posterior U.S. emissions remain relatively close to the prior inventories overall. Our estimates broadly agree with the top-down study of Hu et al. (2017), particularly for HFC-32 and HFC-125, although our posterior estimates for HFC-134a and HFC-143a are somewhat lower.

  We demonstrate that U.S. $SF_6$ emissions have been drastically decreasing between 2005 and 2021. A regional inversion study by Hu et al. (2023), showed a very similar declining U.S. emissions trend, however for a shorter period spanning from 2007 to 2018. While the two studies use a very different inversion set-up and do not precisely match in terms of magnitude, they collectively provide clear evidence about the substantial decline in the U.S. $SF_6$ emissions. It implies that U.S. regulations enforced through EPA have great impact on the U.S. $SF_6$ emissions, which is likely underestimated by current inventories. Another shared finding with Hu et al. (2023) is that the U.S. has been under-reporting its $SF_6$ emissions, especially until the early 2010s, before it became mandatory for high emitting industries to declare their $SF_6$ emissions. Nevertheless, given the demonstrated decrease, the U.S. and its regulatory measures could serve as a role model for effectively reducing $SF_6$ emissions.

- **European F-gas emissions**

  European HFC emissions show an overall declining trend during the study period, although the inversion consistently derives substantially higher emissions than the prior inventories. In the regional inversion, total EU-27 HFC emissions decrease from 145.9 to 126.0 Tg $CO_2$-eq $yr^{-1}$ between

This project has received funding from the European Union's Horizon Europe research and innovation programme under grant agreement No 101081395

2015–2016 and 2020–2021, corresponding to a reduction of about 14%. This decline is mainly driven by decreasing emissions of HFC-134a and HFC-143a (high-GWP species), while HFC-32 (a low-GWP species) shows strong growth, increasing by approximately 55% over the same period. Although both posterior and prior show declining total emissions, the prior inventories suggest substantially lower absolute emissions and stronger declines than inferred by the inversion. Posterior emissions remain systematically higher than the prior across most species, particularly for HFC-143a, HFC-125, and HFC-134a. Among the investigated regions, Europe also shows the strongest sensitivity to inversion configuration, including prior assumptions and baseline treatment. A sensitivity regional inversion using REBS-derived baselines reproduce substantially lower emissions as found in the recent studies by Annadate et al. (2025) and De Longueville et al. (2026). However, sensitivity analyses performed here, together with previous findings by Vojta et al. (2022), indicate that REBS tends to overestimate baseline contributions, which consequently drives posterior emissions downward. In contrast, the FP-LCM baseline, used in this study, produces more balanced site-specific biases. At the country scale, the United Kingdom exhibits a strong decline in total HFC emissions, mainly driven by decreasing HFC-134a and HFC-143a emissions, while HFC-32 increases moderately. Germany shows a contrasting behaviour, with nearly stable or slightly increasing total emissions. France exhibits an intermediate behaviour, with declining HFC-134a and HFC-143a emissions partly offset by increasing HFC-32 and HFC-125 emissions. Across all three countries, posterior estimates remain systematically higher than both inventories and recent REBS-based inversion studies, although the temporal evolution is generally consistent. The European HFC trends are broadly consistent with the impact of the EU F-gas Regulation and the gradual phase-down of high-GWP refrigerants. The pronounced decline in HFC-134a and HFC-143a after the mid-2010s, particularly in the UK and France, likely reflects both regulatory pressure and market transitions toward alternative refrigerants. The growth of HFC-32 across Europe similarly reflects the increasing adoption of lower-GWP systems following Kigali-related transitions.

Both our global and regional inversions show that $SF_6$ emissions have declined across the European Union, which we interpret as a direct consequence of the EU F-gas regulations introduced in 2006 and strengthened in 2014. This decline can be also seen for the large emitters Germany, UK, and France. Germany is the largest $SF_6$ emitter in Europe and, therefore, exerts a strong influence on the overall European emission trend. A pronounced emission decrease between 2017 and 2018, apparent in the European totals, is also observed in emission estimates over southern Germany, suggesting that regional mitigation measures were implemented following the entry into force of the 2014 F-gas regulation. The major emission source identified in southern Germany is not represented in the German national inventories, indicating that emissions from soundproof windows are likely overestimated, while industrial sources—particularly those related to $SF_6$ production and recycling in this region — are underestimated (Meixner et al., 2025). Over the study period, German $SF_6$ emissions declined from 182 (155–251) t $yr^{-1}$ in 2005 to 97 (88–104) t $yr^{-1}$ in 2021, and are in relatively good agreement with values reported to the UNFCCC. Also in France, a posteriori emissions decreased from 78 (51–117) t yr−1 in 2005 to 35 (19–54) t yr−1 in 2021, however exceed the reported values over the whole study period. In the UK, $SF_6$ emissions decreased substantially from 68 (47–77) t $yr^{-1}$ in 2008 to 19 (15–26) t $yr^{-1}$ in 2018, a trend that is likely linked to the 2006 EU F-gas regulation, with most restrictions entering into force in 2008. Our inversion results for the UK agree closely (both in magnitude and temporal evolution) with those of Manning et al. (2022), particularly after 2012, when the UK expanded its observational network, leading to reduced uncertainties. This strong agreement demonstrates the potential of inverse modelling to derive reliable emission estimates when supported by a dense monitoring system, and it underscores the importance of further expanding existing observational networks (e.g., Weiss et al. (2021)). The expansion of the UKs observational system and the inclusion of the inverse modelling results from Manning et al. (2022) in the United Kingdom's annual UNFCCC submissions provides a clear example

This project has received funding from the European Union's Horizon Europe research and innovation programme under grant agreement No 101081395

of how top-down approaches can enhance the accuracy and credibility of national self-reporting, as previously suggested by Rypdal et al. (2005).

Our findings indicate that regulations, such as those implemented by the US. or the EU for F-gases, can help reduce regional GHG emissions. Considering the substantial regional emission reductions observed, the US and Europe could serve as a role-model for effectively reducing US regional F-gas emissions. Similar regulations would be crucial in other regions for mitigating global emissions (e.g., Vojta et al., 2024; An et al., 2024). Furthermore, expanding observation networks – similar to the dense British network – should be a top priority, as this would greatly reduce uncertainties in top-down emission estimates derived from inverse modelling. These improved estimates could then be incorporated into national reports, as already done by Switzerland, the UK, and Australia (e.g. Rypdal et al. (2005) and Leip et al. (2018)), substantially enhancing our understanding of GHG emissions.

While the present results represent our best estimates based on the current inversion framework and have been finalized in line with reporting timelines and their possible extensions, ongoing work is still being carried out to further evaluate their robustness. In particular, additional sensitivity analyses related to initial conditions, transport representation, and other key components of the inversion system are currently underway. These tests aim to quantify the potential impact of methodological choices on the inferred emission estimates and to further strengthen confidence in the reported results.

This project has received funding from the European Union's Horizon Europe research and innovation programme under grant agreement No 101081395

## 5. References

An, M., Prinn, R. G., Western, L. M., Zhao, X., Yao, B., Hu, J., Ganesan, A. L., Mühle, J., Weiss, R. F., and Krummel, P. B.: Sustained growth of sulfur hexafluoride emissions in China inferred from atmospheric observations, Nature Communications, 15, 1997, https://doi.org/10.1038/s41467-024-46084-3, 2024.

Annadate, S., Mancinelli, E., Gonella, B., Moricci, F., O'Doherty, S., Stanley, K., Young, D., Vollmer, M. K., Cesari, R., and Falasca, S.: Monitoring the impact of EU F-gas regulation on HFC-134a emissions through a comparison of top-down and bottom-up estimates, Environmental Sciences Europe, 37, 1-12, https://doi.org/10.1186/s12302-025-01081-1, 2025.

Bakels, L., Tatsii, D., Tipka, A., Thompson, R., Dütsch, M., Blaschek, M., Seibert, P., Baier, K., Bucci, S., and Cassiani, M.: FLEXPART version 11: Improved accuracy, efficiency, and flexibility, Geoscientific Model Development, 17, 7595-7627, https://doi.org/10.5194/gmd-17-7595-2024, 2024.

BEIS: 2020 UK greenhouse gas emissions, final figures, Department for Business, Energy and Industrial Strategy London, UK, 2022.

Bergamaschi, P., Corazza, M., Karstens, U., Athanassiadou, M., Thompson, R. L., Pison, I., Manning, A. J., Bousquet, P., Segers, A., and Vermeulen, A.: Top-down estimates of European CH 4 and N 2 O emissions based on four different inverse models, Atmospheric Chemistry and Physics, 15, 715-736, https://doi.org/10.5194/acp-15-715-2015, 2015.

Brunner, D., Arnold, T., Henne, S., Manning, A., Thompson, R. L., Maione, M., O'Doherty, S., and Reimann, S.: Comparison of four inverse modelling systems applied to the estimation of HFC-125, HFC-134a, and SF 6 emissions over Europe, Atmospheric Chemistry and Physics, 17, 10651-10674, https://doi.org/10.5194/acp-17-10651-2017, 2017.

Chevallier, F., Remaud, M., O'Dell, C. W., Baker, D., Peylin, P., and Cozic, A.: Objective evaluation of surface-and satellite-driven carbon dioxide atmospheric inversions, Atmospheric Chemistry and Physics, 19, 14233-14251, https://doi.org/10.5194/acp-19-14233-2019, 2019.

Crippa, M., Guizzardi, D., Pagani, F., Banja, M., Muntean, M., Schaaf, E., Becker, W., Monforti-Ferrario, F., Quadrelli, R., and Risquez Martin, A.: GHG emissions of all world countries, Publications Office of the European Union, Luxembourg, 10, 953322, https://doi.org/10.2760/9816914., 2023.

Cui, Z., Li, Y., Xiao, S., Tian, S., Tang, J., Hao, Y., and Zhang, X.: Recent progresses, challenges and proposals on SF6 emission reduction approaches, Science of The Total Environment, 906, 167347, https://doi.org/10.1016/j.scitotenv.2023.167347, 2024.

Cunnold, D., Prinn, R., Rasmussen, R., Simmonds, P., Alyea, F., Cardelino, C., Crawford, A., Fraser, P., and Rosen, R.: The Atmospheric Lifetime Experiment: 3. Lifetime methodology and application to three years of CFCl3 data, Journal of Geophysical Research: Oceans, 88, 8379-8400, https://doi.org/10.1029/JC088iC13p08379, 1983.

De Longueville, H., Melo, D. B., Redington, A., Ramsden, A., Danjou, A., Andrews, P., Pitt, J., Murphy, B., Constantin, L., and Stanley, K. M.: European HFC emissions evaluated with multiple atmospheric inverse models and UNFCCC national inventories, EGUsphere, 2026, 1-40, https://doi.org/10.5194/egusphere-2026-194, 2026 preprint.

De Longueville, H., Melo, D. B., Redington, A. L., Ramsden, A., Danjou, A., Andrews, P., Pitt, J., Murphy, B., Constantin, L., and Stanley, K. M.: European HFC emissions evaluated with multiple atmospheric inverse models and UNFCCC national inventories, Atmospheric Chemistry and Physics, 26, 7647-7675, 2026.

This project has received funding from the European Union's Horizon Europe research and innovation programme under grant agreement No 101081395

Fang, X., Du, Q., Mühle, J., Hu, J., Weiss, R. F., Prinn, R. G., Harth, C. M., O'Doherty, S., Young, D., and Ma, M.: Estimation of hydrofluorocarbon emissions from China and other non-Annex I countries, Nature Geoscience, 1-8, https://doi.org/10.1038/s41561-025-01908-9, 2026.

Fang, X., Thompson, R. L., Saito, T., Yokouchi, Y., Kim, J., Li, S., Kim, K., Park, S., Graziosi, F., and Stohl, A.: Sulfur hexafluoride (SF 6) emissions in East Asia determined by inverse modeling, Atmospheric Chemistry and Physics, 14, 4779-4791, https://doi.org/10.5194/acp-14-4779-2014, 2014.

Flerlage, H., Velders, G. J., and de Boer, J.: A review of bottom-up and top-down emission estimates of hydrofluorocarbons (HFCs) in different parts of the world, Chemosphere, 283, 131208, https://doi.org/10.1016/j.chemosphere.2021.131208, 2021.

Ganesan, A., Rigby, M., Zammit-Mangion, A., Manning, A., Prinn, R., Fraser, P., Harth, C., Kim, K.-R., Krummel, P., and Li, S.: Characterization of uncertainties in atmospheric trace gas inversions using hierarchical Bayesian methods, Atmospheric Chemistry and Physics, 14, 3855-3864, 2014.

Ganesan, A., Manning, A., Barrigar, O., Bovensmann, H., Brailsford, G., Brunner, D., Bukosa, B., Emmenegger, L., Henne, S., Reimann, S., and al., e.: IG3IS Guidance for Estimating National-scale Greenhouse Gas Emissions using Atmospheric Observations, GAW Report No. 319, 2025.

Glaesmann, N.: Marktanalyse und Bedeutung von Wärmepumpenheizungen, in: Wärmepumpenheizungen: Planungshilfe und Ratgeber für Neubauten und Bestandsgebäude, Springer, 17-25, https://doi.org/10.1007/978-3-658-39031-0, 2023.

Groot Zwaaftink, C. D., Henne, S., Thompson, R. L., Dlugokencky, E. J., Machida, T., Paris, J.-D., Sasakawa, M., Segers, A., Sweeney, C., and Stohl, A.: Three-dimensional methane distribution simulated with FLEXPART 8-CTM-1.1 constrained with observation data, Geoscientific Model Development, 11, 4469-4487, https://doi.org/10.5194/gmd-11-4469-2018, 2018.

Guillevic, M., Vollmer, M. K., Wyss, S. A., Leuenberger, D., Ackermann, A., Pascale, C., Niederhauser, B., and Reimann, S.: Dynamic–gravimetric preparation of metrologically traceable primary calibration standards for halogenated greenhouse gases, Atmospheric Measurement Techniques, 11, 3351-3372, https://doi.org/10.5194/amt-11-3351-2018, 2018.

Guo, L., Yang, Y., Fraser, P. J., Velders, G. J., Liu, Z., Cui, D., Quan, J., Cai, Z., Yao, B., and Hu, J.: Projected increases in emissions of high global warming potential fluorinated gases in China, Communications Earth & Environment, 4, 205, https://doi.org/10.1038/s43247-023-00859-6, 2023.

Helton, J. C. and Davis, F. J.: Latin hypercube sampling and the propagation of uncertainty in analyses of complex systems, Reliability Engineering & System Safety, 81, 23-69, https://doi.org/10.1016/S0951-8320(03)00058-9, 2003.

Henne, S., Brunner, D., Groot Zwaaftink, C., and Stohl, A.: FLEXPART 8-CTM-1.1: Atmospheric Lagrangian Particle Dispersion Model for global tracer transport, Zenodo, https://doi.org/10.5194/gmd-11-4469-2018, 2018.

Hersbach, H., Bell, B., Berrisford, P., Hirahara, S., Horányi, A., Muñoz-Sabater, J., Nicolas, J., Peubey, C., Radu, R., and Schepers, D.: The ERA5 global reanalysis, Quarterly journal of the royal meteorological society, 146, 1999-2049, https://doi.org/10.1002/qj.3803, 2020.

Hu, L., Montzka, S. A., Lehman, S. J., Godwin, D. S., Miller, B. R., Andrews, A. E., Thoning, K., Miller, J. B., Sweeney, C., and Siso, C.: Considerable contribution of the Montreal Protocol to declining greenhouse gas emissions from the United States, Geophysical Research Letters, 44, 8075-8083, https://doi.org/10.1002/2017GL074388, 2017.

Hu, L., Ottinger, D., Bogle, S., Montzka, S. A., DeCola, P. L., Dlugokencky, E., Andrews, A., Thoning, K., Sweeney, C., and Dutton, G.: Declining, seasonal-varying emissions of sulfur hexafluoride from the

This project has received funding from the European Union's Horizon Europe research and innovation programme under grant agreement No 101081395

United States, Atmospheric Chemistry and Physics, 23, 1437-1448, https://doi.org/10.5194/acp-23-1437-2023, 2023.

Katharopoulos, I., Rust, D., Vollmer, M. K., Brunner, D., Reimann, S., O'Doherty, S. J., Young, D., Stanley, K. M., Schuck, T., and Arduini, J.: Impact of transport model resolution and a priori assumptions on inverse modeling of Swiss F-gas emissions, Atmospheric Chemistry and Physics, 23, 14159-14186, https://doi.org/10.5194/acp-23-14159-2023, 2023.

Kikstra, J. S., Nicholls, Z. R., Smith, C. J., Lewis, J., Lamboll, R. D., Byers, E., Sandstad, M., Meinshausen, M., Gidden, M. J., and Rogelj, J.: The IPCC Sixth Assessment Report WGIII climate assessment of mitigation pathways: from emissions to global temperatures, Geoscientific Model Development, 15, 9075-9109, https://doi.org/10.5194/gmd-15-9075-2022, 2022.

Leip, A., Skiba, U., Vermeulen, A., and Thompson, R. L.: A complete rethink is needed on how greenhouse gas emissions are quantified for national reporting, Atmospheric Environment, 174, 237-240, https://doi.org/10.1016/j.atmosenv.2017.12.006, 2018.

Locatelli, R., Bousquet, P., Chevallier, F., Fortems-Cheney, A., Szopa, S., Saunois, M., Agusti-Panareda, A., Bergmann, D., Bian, H., and Cameron-Smith, P.: Impact of transport model errors on the global and regional methane emissions estimated by inverse modelling, Atmospheric Chemistry and Physics, 13, 9917-9937, https://doi.org/10.5194/acp-13-9917-2013, 2013.

Lucas, D. D., Simpson, M., Cameron-Smith, P., and Baskett, R. L.: Bayesian inverse modeling of the atmospheric transport and emissions of a controlled tracer release from a nuclear power plant, Atmospheric Chemistry and Physics, 17, 13521-13543, https://doi.org/10.5194/acp-17-13521-2017, 2017.

Manning, A., O'Doherty, S., Jones, A., Simmonds, P., and Derwent, R.: Estimating UK methane and nitrous oxide emissions from 1990 to 2007 using an inversion modeling approach, Journal of Geophysical Research: Atmospheres, 116, https://doi.org/10.1029/2010JD014763, 2011.

Manning, A. J., Redington, A. L., Say, D., O'Doherty, S., Young, D., Simmonds, P. G., Vollmer, M. K., Mühle, J., Arduini, J., and Spain, G.: Evidence of a recent decline in UK emissions of hydrofluorocarbons determined by the InTEM inverse model and atmospheric measurements, Atmospheric Chemistry and Physics, 21, 12739-12755, https://doi.org/10.5194/acp-21-12739-2021, 2021.

Meixner, K., Wagenhäuser, T., Schuck, T. J., Alber, S., Manning, A. J., Redington, A. L., Stanley, K. M., O'Doherty, S., Young, D., and Pitt, J.: Characterization of German SF6 Emissions, ACS Es&t Air, 2, 2889-2899, 2025.

NOAA-ESRL: Sulfur Hexafluoride (SF6) WMO Scale, (https://gml.noaa.gov/ccl/sf6_scale.html, last access: 2026-05-21), 2014.

Ottinger, D., Averyt, M., and Harris, D.: US consumption and supplies of sulphur hexafluoride reported under the greenhouse gas reporting program, Journal of Integrative Environmental Sciences, 12, 5-16, https://doi.org/10.1080/1943815X.2015.1092452, 2015.

Park, H., Kim, J., Choi, H., Geum, S., Kim, Y., Thompson, R. L., Mühle, J., Salameh, P. K., Harth, C. M., and Stanley, K. M.: A rise in HFC-23 emissions from eastern Asia since 2015, Atmospheric Chemistry and Physics, 23, 9401-9411, https://doi.org/10.5194/acp-23-9401-2023, 2023.

Prinn, R. G., Weiss, R. F., Arduini, J., Arnold, T., DeWitt, H. L., Fraser, P. J., Ganesan, A. L., Gasore, J., Harth, C. M., and Hermansen, O.: History of chemically and radiatively important atmospheric gases from the Advanced Global Atmospheric Gases Experiment (AGAGE), Earth System Science Data Discussions, 2018, 1-39, https://doi.org/10.5194/essd-10-985-2018, 2018.

This project has received funding from the European Union's Horizon Europe research and innovation programme under grant agreement No 101081395

Purohit, P. and Höglund-Isaksson, L.: Global emissions of fluorinated greenhouse gases 2005–2050 with abatement potentials and costs, Atmospheric Chemistry and Physics, 17, 2795-2816, https://doi.org/10.5194/acp-17-2795-2017, 2017.

Püschel, B., Vojta, M., Kandler, L., Crotwell, M., Engel, A., Krummel, P. B., Lunder, C. R., Mühle, J., O'Doherty, S., and Prinn, R. G.: Global distribution of tetrafluoromethane (CF 4) and hexafluoroethane (C 2 F 6) emissions determined by inverse modeling, EGUsphere, 2025, 1-30, https://doi.org/10.5194/egusphere-2025-5656, 2025.

Rigby, M., Prinn, R., O'doherty, S., Miller, B., Ivy, D., Mühle, J., Harth, C., Salameh, P., Arnold, T., and Weiss, R.: Recent and future trends in synthetic greenhouse gas radiative forcing, Geophysical Research Letters, 41, 2623-2630, https://doi.org/10.1002/2013GL059099, 2014.

Rigby, M., Prinn, R., O'Doherty, S., Montzka, S., McCulloch, A., Harth, C., Mühle, J., Salameh, P., Weiss, R., and Young, D.: Re-evaluation of the lifetimes of the major CFCs and CH 3 CCl 3 using atmospheric trends, Atmospheric Chemistry and Physics, 13, 2691-2702, https://doi.org/10.5194/acp-13-2691-2013, 2013.

Rypdal, K., Stordal, F., Fuglestvedt, J., and Berntsen, T.: Introducing top-down methods in assessing compliance with the Kyoto Protocol, Climate Policy, 5, 393-405, https://doi.org/10.1080/14693062.2005.9685565, 2005.

Simmonds, P. G., Rigby, M., Manning, A. J., Park, S., Stanley, K. M., McCulloch, A., Henne, S., Graziosi, F., Maione, M., and Arduini, J.: The increasing atmospheric burden of the greenhouse gas sulfur hexafluoride (SF 6), Atmospheric Chemistry and Physics, 20, 7271-7290, https://doi.org/10.5194/acp-20-7271-2020, 2020.

Simmonds, P. G., Rigby, M., McCulloch, A., Vollmer, M. K., Henne, S., Mühle, J., O'Doherty, S., Manning, A. J., Krummel, P. B., and Fraser, P. J.: Recent increases in the atmospheric growth rate and emissions of HFC-23 (CHF 3) and the link to HCFC-22 (CHClF 2) production, Atmospheric Chemistry and Physics, 18, 4153-4169, https://doi.org/10.5194/acp-18-4153-2018, 2018.

Stohl, A., Seibert, P., Arduini, J., Eckhardt, S., Fraser, P., Greally, B., Lunder, C., Maione, M., Mühle, J., and O'doherty, S.: An analytical inversion method for determining regional and global emissions of greenhouse gases: Sensitivity studies and application to halocarbons, Atmospheric Chemistry and Physics, 9, 1597-1620, 2009.

Thacker, W.: Data assimilation with inequality constraints, Ocean Modelling, 16, 264-276, https://doi.org/10.1016/j.ocemod.2006.11.001, 2007.

Thompson, R. L. and Stohl, A.: FLEXINVERT: an atmospheric Bayesian inversion framework for determining surface fluxes of trace species using an optimized grid, Geoscientific Model Development, 7, 2223-2242, https://doi.org/10.5194/gmd-7-2223-2014, 2014.

UNEP: REPORT OF THE TECHNOLOGY AND ECONOMIC ASSESSMENT PANEL SEPTEMBER (https://ozone.unep.org/hfc-23-emissions, last access: 11/02/2026), 2024.

Vimont, I., Montzka, S., & Elkins, J.: NOAA Global Monitoring Laboratory, (https://gml.noaa.gov, last access: 12.02.2025), 2015.

Vojta, M., Plach, A., Thompson, R. L., and Stohl, A.: A comprehensive evaluation of the use of Lagrangian particle dispersion models for inverse modeling of greenhouse gas emissions, Geoscientific Model Development, 15, 8295-8323, https://doi.org/10.5194/gmd-15-8295-2022, 2022.

Vojta, M., Plach, A., Annadate, S., Park, S., Lee, G., Purohit, P., Lindl, F., Lan, X., Mühle, J., and Thompson, R. L.: A global re-analysis of regionally resolved emissions and atmospheric mole fractions

This project has received funding from the European Union's Horizon Europe research and innovation programme under grant agreement No 101081395

of SF6 for the period 2005–2021, Atmospheric Chemistry and Physics, 24, 12465-12493, https://doi.org/10.5194/egusphere-2024-811, 2024.

Vojta, M., Plach, A., Thompson, R. L., Purohit, P., Stanley, K., O'Doherty, S., Young, D., Pitt, J., Arduini, J., and Lan, X.: Quantifying European SF6 emissions from 2005 to 2021 using a large inversion ensemble, Atmospheric Chemistry and Physics, 25, 15197-15243, https://doi.org/10.5194/acp-25-15197-2025, 2025.

Weiss, R. F., Ravishankara, A., and Newman, P. A.: Huge gaps in detection networks plague emissions monitoring, Nature, 595, 491-493, https://doi.org/10.1038/d41586-021-01967-z, 2021.

Western, L. M., Rigby, M., Mühle, J., Krummel, P. B., Lunder, C. R., O'doherty, S., Reimann, S., Vollmer, M. K., Young, D., and Adam, B.: Global emissions and abundances of chemically and radiatively important trace gases from the AGAGE network, Earth System Science Data Discussions, 2025, 1-41, 2025.

Wu, J., Wang, T., An, M., Ding, S., Yao, B., Western, L. M., Purohit, P., Liu, Z., Zhang, Z., and Peng, L.: Development and validation of a gridded emissions inventory for HFC-134a in China, Environment International, 109535, https://doi.org/10.1016/j.envint.2025.109535, 2025.

Yao, B., Fang, X., Vollmer, M. K., Reimann, S., Chen, L., Fang, S., and Prinn, R. G.: China's hydrofluorocarbon emissions for 2011–2017 inferred from atmospheric measurements, Environmental Science & Technology Letters, 6, 479-486, 2019.

EU: Directive 2006/40/EC of the European Parliament and of the Council of 17 May 2006 relating to emissions from air-conditioning systems in motor vehicles and amending Council Directive 70/156/EEC, Official Journal of the European Union, L 161, 14 June 2006, pp. 12–18. CELEX: 32006L0040. https://eur-lex.europa.eu/eli/dir/2006/40/oj (last access: 25 May 2026), 2006

EU: Regulation (EC) No 842/2006 of the European Parliament and of the Council of 17 May 2006 on Certain Fluorinated Greenhouse Gases, Official Journal of the European Union: Luxembourg, https://eur-lex.europa.eu/legal-content/EN/TXT/PDF/?uri=CELEX:32006R0842 (last access: 1 January 2026), 2006

EU: Regulation (EU) No. 517/2014 of the European Parliament and of the Council of 16 April 2014 on fluorinated greenhouse gases and repealing Regulation (EC) No. 842/2006. Official Journal of the European Union, L 150/195, Luxembourg, https://eur-lex.europa.eu/legal-content/EN/TXT/PDF/?uri=CELEX:32014R0517 (last access: 1 January 2026), 2014.

EU: Regulation (EU) 2024/590 of the European Parliament and of the Council of 7 February 2024 on Substances That Deplete the Ozone Layer, and Repealing Regulation (EC) No 1005/2009, Official Journal of the European Union: Luxembourg, https://eur-lex.europa.eu/legal-content/EN/TXT/PDF/?uri=CELEX:32024R0590 (last access: 1 January 2026), 2024.

Manning, A., Redington, A., O'Doherty, S., Say, D., Young, D., Arnold, T., Rennick, C., Rigby, M., Wisher, A., and Simmonds, P.: Long-Term Atmospheric Measurement and Interpretation of Radiatively Active Trace Gases–Detailed Report (September 2019 to August 2020), Tech. rep., Department for Business, Energy & Industrial Strategy, https://assets.publishing.service.gov.uk/media, (last access: 1 January 2026), 2022.

WMO: Ozone Research and Monitoring – GAW Report No. 278, GAW Report 278, World Meteorological Organization, Geneva, Switzerland, https://ozone.unep.org/sites/default/files/2023-02/Scientific-Assessment-of-Ozone-Depletion-2022.pdf (last accessed: 28 January 2026), 2022.

This project has received funding from the European Union's Horizon Europe research and innovation programme under grant agreement No 101081395

# 6. Supplementary Material

## 6.1 Reduction in uncertainty derived from the inversion

The global patterns of uncertainty reduction for HFCs, specifically HFC-134a, HFC-143a, HFC-32, and HFC-125, are similar, contrasting with HFC-23. Figure S1 highlights this difference for HFC-134a and HFC-23 in 2022 (patterns for the other HFCs and SF6 are in Fig. S2). This difference stems primarily from variations in observational coverage. HFC-134a, HFC-143a, HFC-32, and HFC-125 are monitored by both high- and low-frequency sites across major global emission sources. In addition to the inherent challenges of monitoring HFC-23, which is primarily emitted from industrial point sources, observations are available from only a few high-frequency global stations, resulting in sparse spatial coverage. This uneven sampling significantly impacts emission constraint in the US, particularly in the eastern region, where HFC monitoring relies almost exclusively on low-frequency NOAA stations (Figure 4). Secondly, the spatial distribution of HFC-23 emission sources differs considerably from the other studied HFCs, with a notable, different concentration over Russia. As suggested by Equation (5), HFC-23's relatively strong uncertainty reduction in eastern Russia arises from a substantial emission source, which produces high prior uncertainty and allows the inversion to make a significant update, rather than from improved observational coverage in a poorly monitored area (Figure 4). Although emissions are high over India, parts of West Asia, Africa, and South America, poor observational coverage results in near-zero uncertainty reductions and unreliable posterior estimates. For SF6 global patterns of uncertainty reduction look similar to those of HFC-134a, HFC-143a, HFC-32, and HFC-125 in the US and Europe, however, align closer with HFC-23 in East China due to large a priori emission in this region.

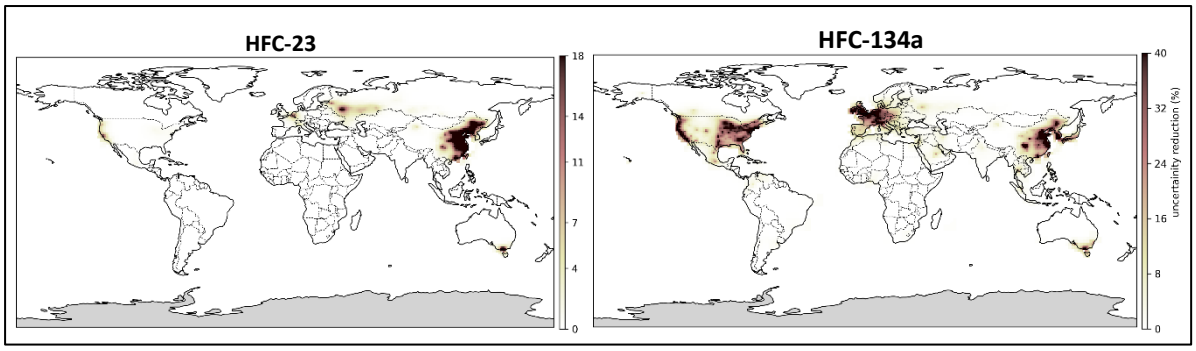


*Figure S1: Median relative uncertainty reduction (%) = median [(1 − Posterior error / Prior error) × 100] for HFC-134a and HFC-23 through study period. Results for other HFCs and SF6 are available in Figure S2.*

This project has received funding from the European Union's Horizon Europe research and innovation programme under grant agreement No 101081395

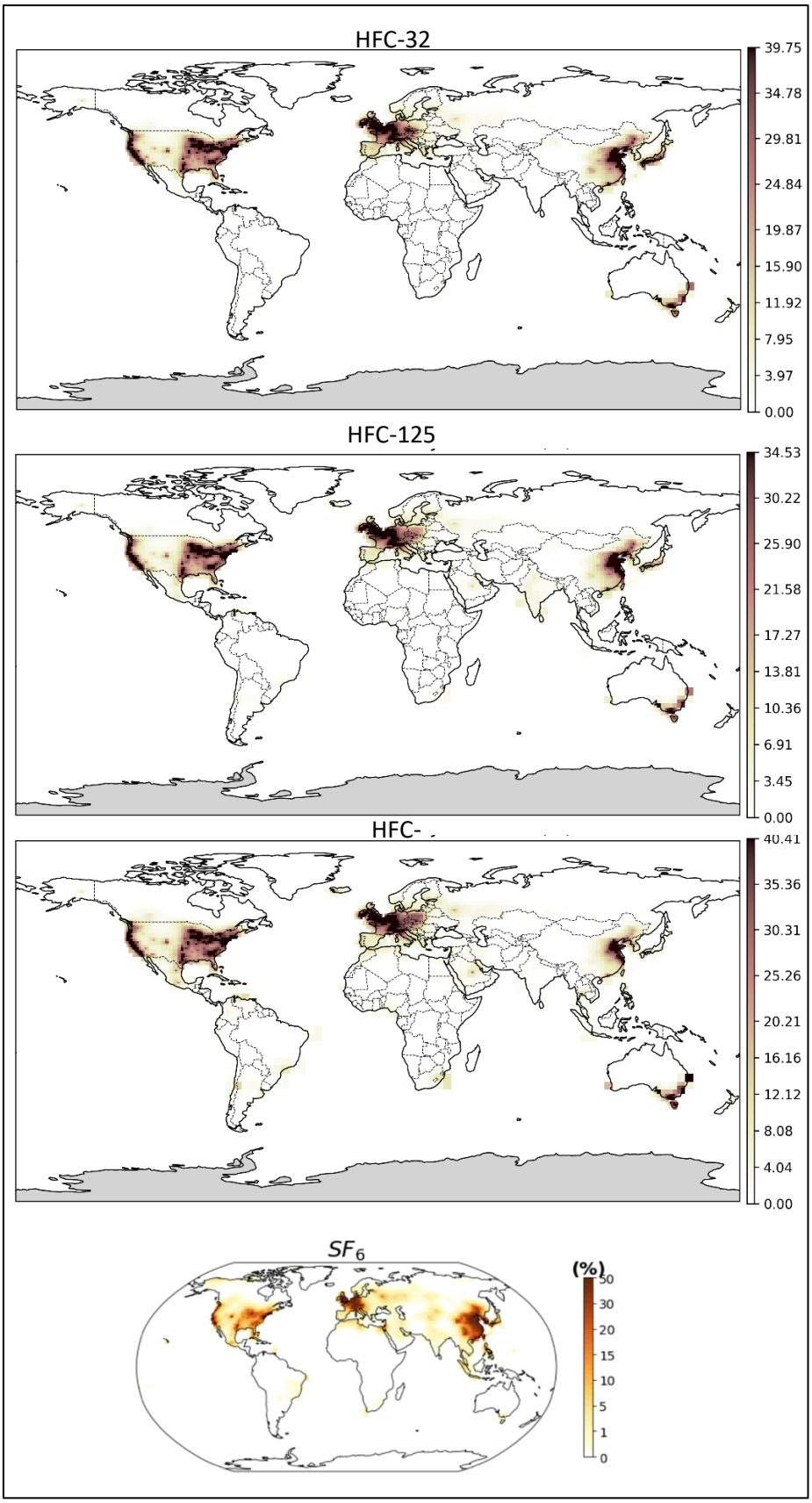


*Figure S2: Median relative uncertainty reduction (%) = median [(1 − Posterior error / Prior error) × 100] for HFC-32, HFC-125, HFC-143a, and SF6 through study period.*

This project has received funding from the European Union's Horizon Europe research and innovation programme under grant agreement No 101081395

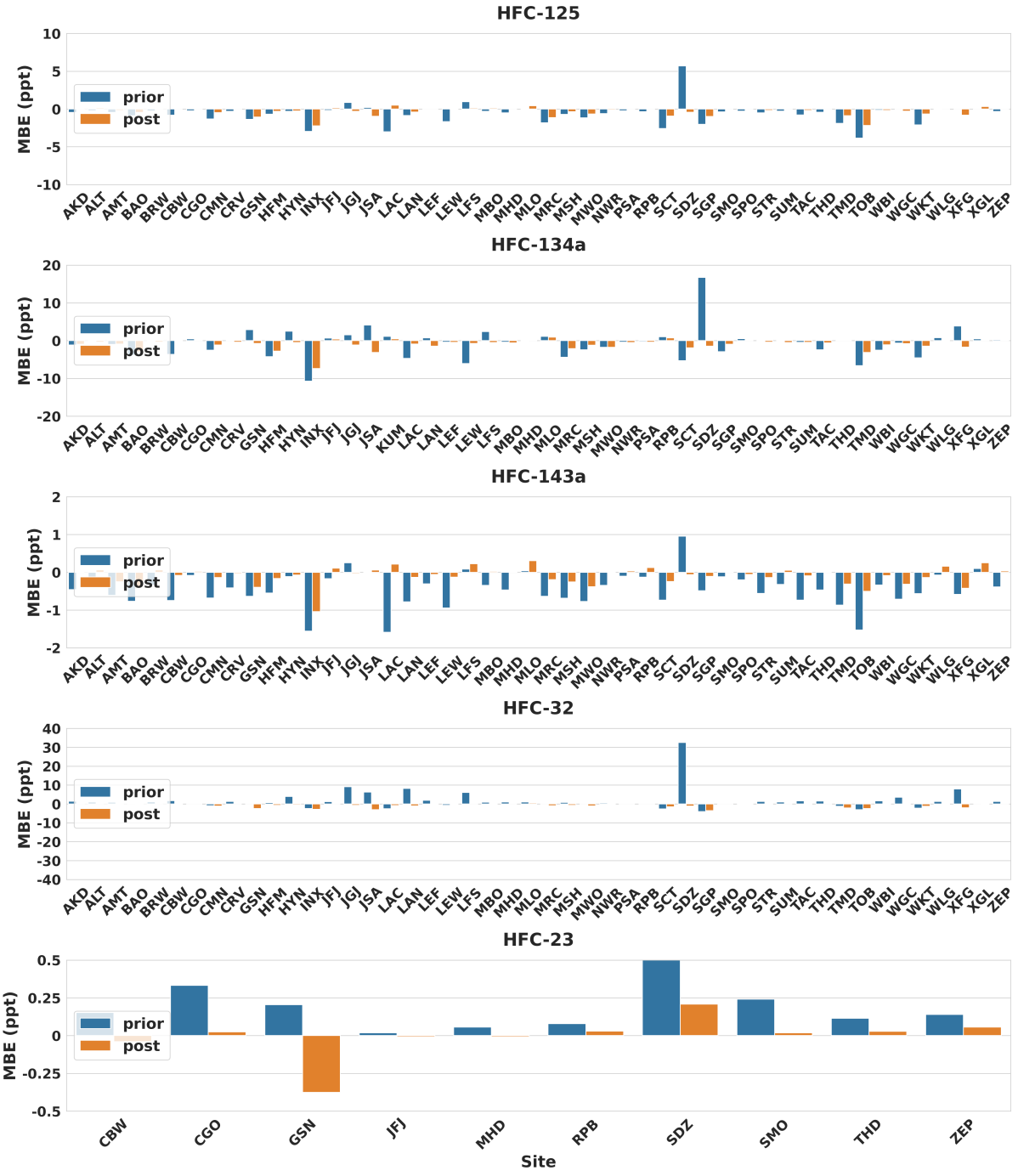


*Figure S3. Same as Fig. 9, but showing MBE for all stations before and after the inversion. The metric calculation was performed on a representative run selected to reflect the median of estimates for each species and year based on country totals. Specifically, for each ensemble member, country totals were computed, and the Euclidean distance of that member to the median country totals was calculated. The run with the smallest distance was then chosen for the performance analysis presented here.*

This project has received funding from the European Union's Horizon Europe research and innovation programme under grant agreement No 101081395

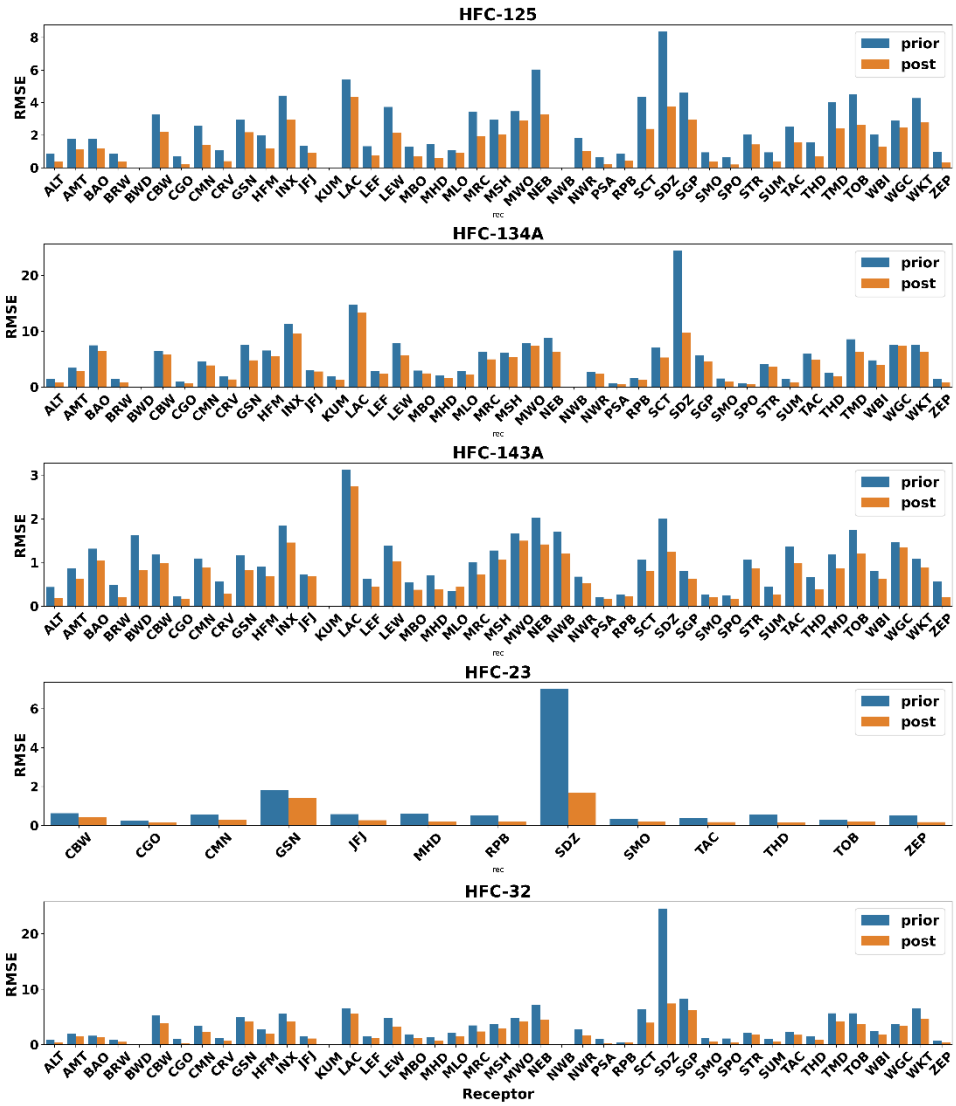


*Figure S4. Same as Fig. 9, but showing RMSE for all stations before and after the inversion. The metric calculation was performed on a representative run selected to reflect the median of estimates for each species and year based on country totals. Specifically, for each ensemble member, country totals were computed, and the Euclidean distance of that member to the median country totals was calculated. The run with the smallest distance was then chosen for the performance analysis presented here.*

This project has received funding from the European Union's Horizon Europe research and innovation programme under grant agreement No 101081395

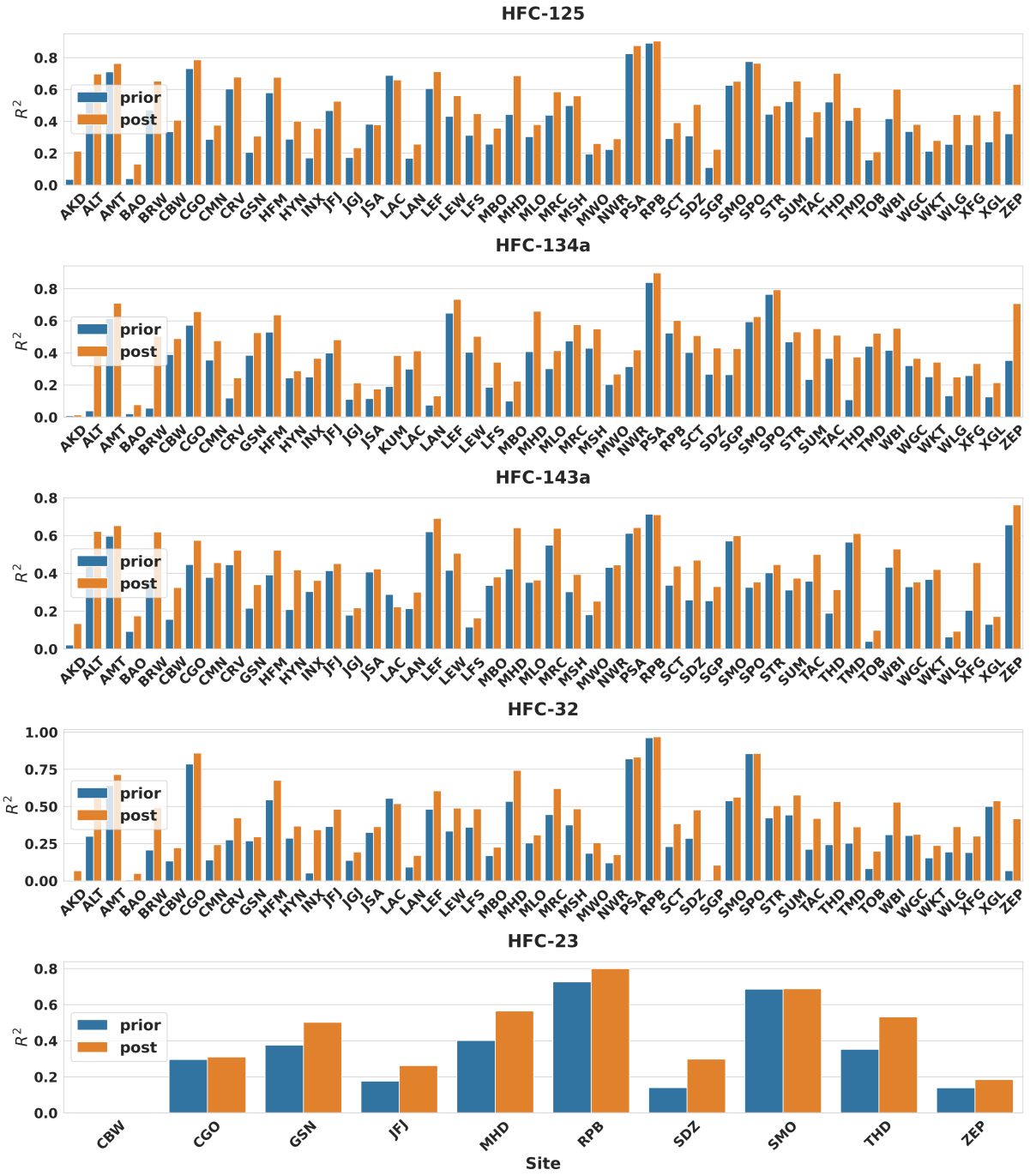


*Figure S5. Same as Fig. 9, but showing coefficient of determination for all stations before and after inversion: The metric calculation was performed on a representative run selected to reflect the median of estimates for each species and year based on country totals. Specifically, for each ensemble member, country totals were computed, and the Euclidean distance of that member to the median country totals was calculated. The run with the smallest distance was then chosen for the performance analysis presented here.*

This project has received funding from the European Union's Horizon Europe research and innovation programme under grant agreement No 101081395

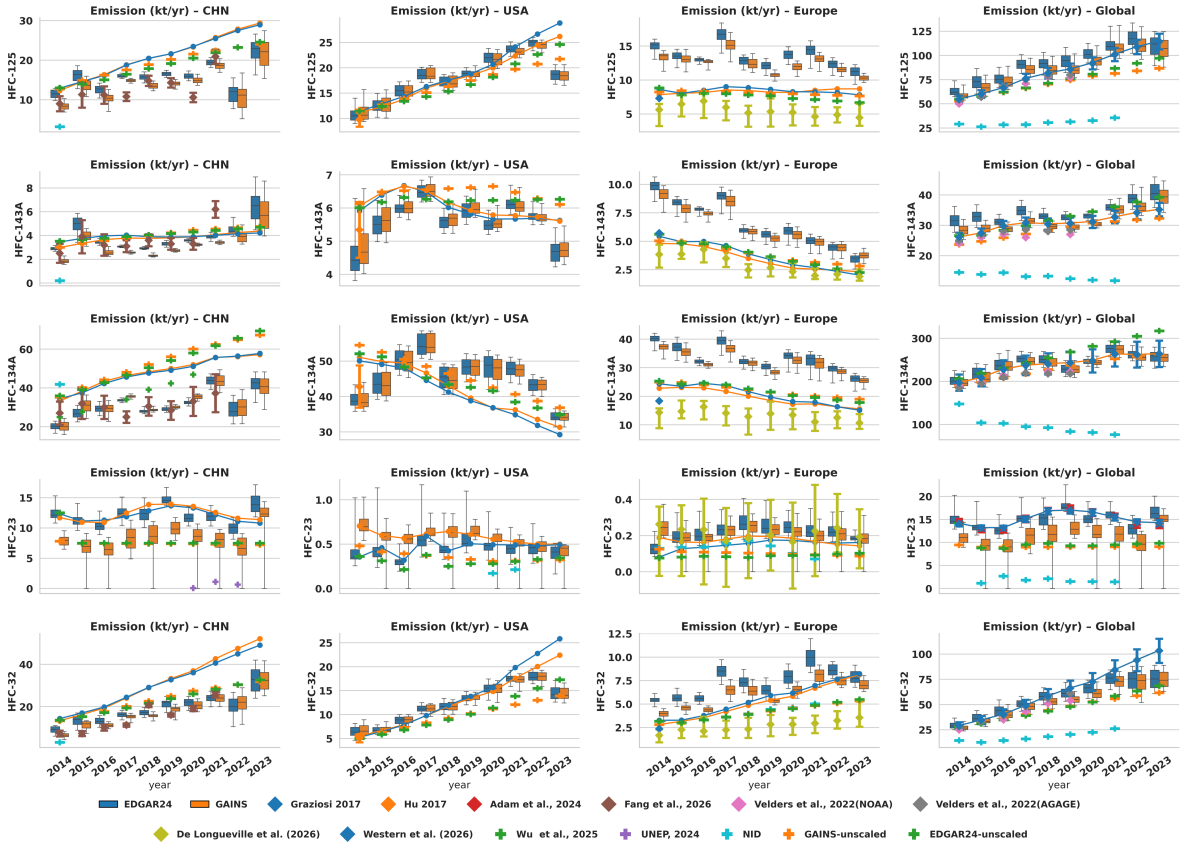


*Figure S6. Time series of HFC posterior estimates for major emitting regions, separated by prior.*

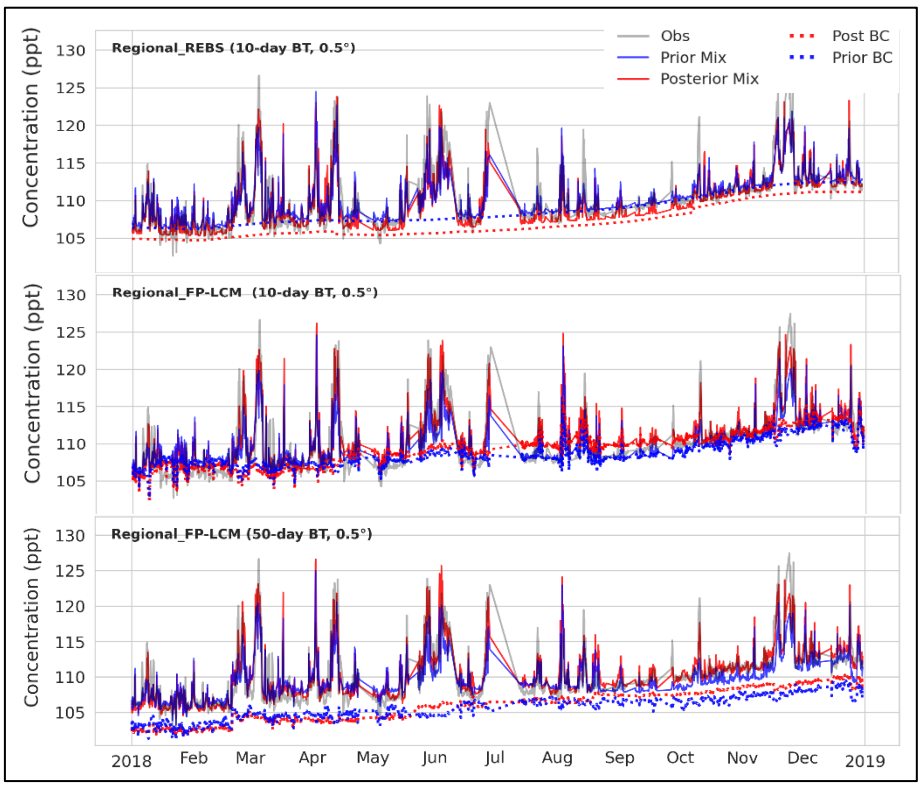


*Figure S7. Time series of observed and modelled HFC-134a concentrations at MHD using REBS and FP-LCM with 10-day backward trajectories (top and middle panels, respectively), and FP-LCM with 50-day backward trajectories (bottom panel).*

This project has received funding from the European Union's Horizon Europe research and innovation programme under grant agreement No 101081395

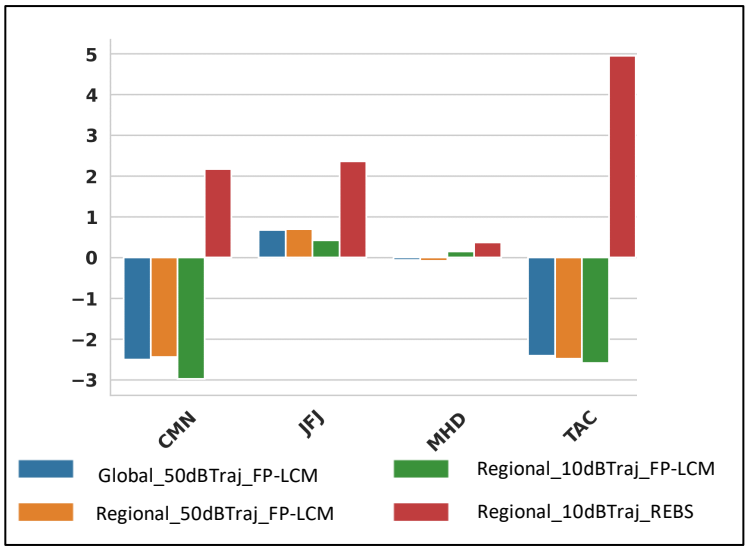


*Figure S8. Same as Fig. 15-B, but with the additional inclusion of global and regional simulations using 50-day backward trajectories.*

This project has received funding from the European Union's Horizon Europe research and innovation programme under grant agreement No 101081395

https://eyeclima.eu

BRUSSELS, 02 07 2026

*Funded by the European Union. Views and opinions expressed are however those of the author(s) only and do not necessarily reflect those of the European Union. Neither the European Union nor the granting authority can be held responsible for them.*

This project has received funding from the European Union's Horizon Europe research and innovation programme under grant agreement No 101081395